# Optical Negative Index Metamaterials

by

Xuhuai Zhang

A dissertation submitted in partial fulfillment
of the requirements for the degree of
Doctor of Philosophy
(Physics)
In The University of Michigan
2011

Doctoral Committee:

Professor Stephen R. Forrest, Chair
Professor Paul R. Berman
Professor Duncan G. Steel
Professor Herbert G. Winful

“Science requires the absolute honesty about acquired data and the intellectual honesty that insists on resolving logical contradictions.”

“Skeptical testing and retesting of ideas is central to the way science works.”

“Scientists must be open to new ideas and ready to modify their opinions if and when contradictory evidence emerges.”

-H. Quinn, “What is science?” *Physics Today* 62**,** 8 2009

---

2011

# Acknowledgements

First and foremost, I would like to thank my advisor Prof. Stephen Forrest for guidance and patience throughout my doctoral research. As far as I understand, his philosophy of being a physicist is that any theoretical prediction should be experimentally observable. On the other hand, he holds a healthy dose of skepticism for any assumption. These simple yet profound principles that he infuses his students with have resulted in this dissertation. His enthusiasm, rigor, and high standard for work will also benefit me immensely in the future.

I am deeply indebted to Dr. Marcelo Davanço. When I started research on metamaterials, my knowledge of periodic structures was limited, and I knew absolutely nothing about nano-fabrication. I was fortunate to have worked with Marcelo for about two years and received from him substantial hand-holding, without which this dissertation would be impossible.

I also owe great appreciation to Prof. Gennady Shvets and Prof. Xiaoqin Li at the University of Texas at Austin. Prof. Shvets and his group introduced us to the field of metamaterials by discussing a structure with us. Prof. Li and her group performed the challenging interferometry experiment on the fabricated sample.

I would like to thank the committee members for comments. In addition, I deepened my understanding of important concepts such as symmetry and linear response in the classes of Prof. Paul Berman and Prof. Herbert Winful. I still remember the cookies Prof. Berman fed us in the middle of his five-hour-long quantum mechanics final exam years ago. I thank Prof. Duncan Steel for his leniency at my preliminary exam despite my less than satisfactory answers back then. I would also like to acknowledge the enlightening discussions with Prof. Roberto Merlin and Prof. Anthony Grbic.

I learned enormously from other members of the Optoelectronic Components and Materials Group, particularly those who I have worked with: Noel Giebink, Stephane Kena-Cohen, Kuen-Ting Shiu, Ning Li, Gregory Mcgraw, Jeramy Zimmerman, Rhonda Bailey-Salzman, Xin Xu, Yiru Sun, Fan Yang, Richard Lunt, Guodan Wei, Xiaoran Tong, and Kyle Renshaw. Eva Ruff and other group administrators have spared no effort to constantly provide their support.

Although I cannot name and thank all my friends in the College of Engineering, Meng Zhang, Weiming Wang, and Dong Sun have been the most helpful.

Funding from the Air Force Office of Scientific Research, the China Scholarship Council, and the Rackham Predoctoral Fellowship has made this dissertation possible and is gratefully acknowledged.

Finally, I thank my parents, Xinxin and Liangyan, and my girlfriend, Jing. Without their love and support, I would have never finished the journey of a Ph.D. candidate.

# TABLE OF CONTENTS

# List of Figures

# Abstract

Research of metamaterials focuses on unprecedented optical properties that may be obtained from composite media, and has attracted great attention since the seminal paper "Negative Refraction Makes a Perfect Lens". The theory underpinning this field treats electromagnetic composites using homogenization and effective medium theory (EMT). This thesis discusses negative index metamaterials (NIMs) that exhibit negative refraction. The results can be summarized as follows:

1. The refractive index and maximum unit cell size of an *arbitrary* NIM can be determined from its photonic band structure in the zero-loss limit.
2. A *unified, quantitative* explanation can be given to negative refraction observed in both lossy NIMs and lossless photonic crystals.
3. A near-infrared *subwavelength* NIM is demonstrated.
4. There is *no* theoretical basis for constructing a superlens.

We first derive a general relationship between the bulk index of an arbitrary NIM and its photonic band structure and a maximum unit cell size in the zero-loss limit. Based on discrete translational symmetry, we generalize Bloch's theorem to a phase matching condition with a complex transverse wavevector, which provides a unified explanation of negative refraction observed in lossless photonic crystals and lossy NIMs.

A near-infrared NIM using paired metallic strips is also designed and fabricated using electron beam lithography. It operates at a wavelength of 1$\mu$m, and has a ratio of wavelength to periodicity of 7, to our knowledge the highest yet achieved among experimental optical NIMs. The NIM is characterized by scanning electron and atomic force microscopies. Optical transmission and interferometric measurements are also consistent with a bulk negative index derived from band structure.

Finally, a model NIM is designed based on Mie resonances, resulting in an effective medium with $\varepsilon=\mu=-1$ after homogenization. EMT predicts that such a material is capable of perfect lensing, but is found to substantially overestimate the range of recoverable evanescent waves due to neglect of the microstructure. This result explains the fact that the perfect lens has not been demonstrated after a decade of experimental effort.

This dissertation emphasizes the physical behavior of composites, as well as the importance of microscopic models and experiment in metamaterials research.

# CHAPTER 1

## Introduction: Classical Electromagnetism and Metamaterials

Metamaterials comprise a field of research that focuses on electromagnetic composite structures that yield novel phenomena such as a negative refractive index. The design, fabrication, and characterization of these composites, as well as predictions and experimental implementations of their applications, have led to numerous publications in this new field. This chapter introduces the concept of metamaterials and the underlying effective medium theory in a historical context. The description is intended to be logically, rather than technically, complete and thorough. More details can be found in the references.

### 1. 1 Maxwell's Equations and Their Empirical Justification

Classical electromagnetism is described by Maxwell's Equations first published in 1862, which were later rewritten by Heaviside in the more compact form using vector calculus:

$$\begin{aligned}
\nabla \cdot \mathbf{E} &= \frac{\rho}{\varepsilon_0} \\
\nabla \cdot \mathbf{B} &= 0 \\
\nabla \times \mathbf{E} &= -\frac{\partial \mathbf{B}}{\partial t} \\
\nabla \times \mathbf{B} &= \mu_0 \mathbf{J} + \mu_0 \varepsilon_0 \frac{\partial \mathbf{E}}{\partial t}.
\end{aligned} \tag{1.1}$$

These equations are the microscopic form of Maxwell Equations, since $\rho$ and **J** are densities of total charges and currents, including those on the atomic level. These sources of excitation determine the experimental observables of electric field, **E**, and magnetic induction, **B**, and $\varepsilon_0$ and $\mu_0$ are vacuum dielectric constant and magnetic permeability, respectively. Equations 1.1 are therefore also known as "Maxwell's Equations in a vacuum".

However, $\rho$ and **J** in natural materials involve complicated distributions of bound charges and currents due to polarization and magnetization, which are difficult to access directly. Therefore, auxiliary fields **D** (electric displacement field) and **H** (magnetic field) are introduced in macroscopic Maxwell's Equations:

$$\begin{aligned}
\nabla \cdot \mathbf{D} &= \rho_f \\
\nabla \cdot \mathbf{B} &= 0 \\
\nabla \times \mathbf{E} &= -\frac{\partial \mathbf{B}}{\partial t} \\
\nabla \times \mathbf{H} &= \mathbf{J}_f + \frac{\partial \mathbf{D}}{\partial t}.
\end{aligned} \tag{1.2}$$

Here, $\rho_f$ and $\mathbf{J}_\mathrm{f}$ are densities of only free charges and currents. For linear isotropic homogeneous materials, **D** and **H** are related to **E** and **B** through simple constitutive relations:

$$\mathbf{D} = \varepsilon\mathbf{E}$$
$$\mathbf{B} = \mu\mathbf{H}, \tag{1.3}$$

where $\varepsilon$ and $\mu$ are the dielectric constant and magnetic permeability characteristic of the material, respectively. For anisotropic materials, $\varepsilon$ and $\mu$ are represented by tensors.

Macroscopic Maxwell's Equations can be derived from their microscopic counterparts using a procedure that averages the charges and currents on a scale much greater than the inter-atomic spacing, yet still much smaller than the electromagnetic wavelength. An example of such a procedure can be found in Ref. [1]. This treatment, or its various classical or quantum mechanical analogues [2], filter out fluctuations of the electromagnetic field on the atomic scale, and lead to the expressions of $\varepsilon$ and $\mu$ in terms of the average electric and magnetic polarization densities.

In practice, macroscopic Maxwell's Equations are sufficiently accurate for describing *all* macroscopic experimental observations involving conventional dielectrics in nature and are therefore considered exact. This enables experimentalists to characterize $\varepsilon$ and $\mu$ with only one type of measurement, such as ellipsometry. Further, this also allows theorists to use $\varepsilon$ and $\mu$ in these equations as fundamental material properties.

Note, however, that macroscopic Maxwell's Equations replace a physical material with a pair of parameters, $\varepsilon$ and $\mu$, which are constants with no spatial dependence. These equations, therefore model realistic granular materials as structureless continuous media, and are approximate. Furthermore, the averaging procedure assumes that the atomic radius, the detector resolution, and the electromagnetic wavelength are well separated. Macroscopic Maxwell's equations, as well as $\varepsilon$ and $\mu$, are therefore only meaningful for experiments that probe macroscopic electromagnetic fields. These equations are not

applicable to effects with a characteristic length scale approaching atomic or molecular dimensions, such as atomic structure or chemical bonds.

Indeed, the microscopic Maxwell's Equations are also *ab initio* on experimental ground, which are extrapolated from the empirical observations by Coulomb, Biot and Savart, Faraday, and Ampere. "Electromagnetism…developed as an experimental science…The extension of these *macroscopic* laws, even for charges and currents in vacuum, to the *microscopic* domain was for the most part an unjustified extrapolation" [2]. The agreement of microscopic and macroscopic Maxwell's Equations with numerous experimental measurements, however, ultimately justifies these mathematical constructs.

## 1. 2 Metamaterials: Effective Medium Theory and Homogenization

The natural range of $\varepsilon$ and $\mu$ of conventional materials are quite limited. At optical frequencies, for example, large $\varepsilon$ is rare, and usually $\mu$=1 for any natural material. Landau [3] examined the contribution to magnetic susceptibility by atomic and molecular orbitals, and qualitatively explained this lack of high frequency magnetic response as an incompatibility between small atomic dimensions and macroscopic magnetism. Merlin, however, argued [4] that this may not be the case for mesoscopic composite structures. Indeed, since $\varepsilon$ and $\mu$ derive from the averaged electromagnetic response of atoms and molecules, the restriction to a limited range of $\varepsilon$ and $\mu$ may be removed by composites consisting of natural materials, provided they have a characteristic length scale of inhomogeneities still much smaller than the wavelength. An averaging procedure that calculates $\varepsilon$ and $\mu$ of a composite by approximating it as a homogeneous medium is a homogenization theory.

Assuming that these composites, or metamaterials, can be modeled in macroscopic Maxwell equations with $\varepsilon$ and $\mu$ obtained from homogenization, unusual effects may emerge. Such a model for describing metamaterials is known as an effective medium theory (EMT).

Therefore research on metamaterials has two main thrusts, corresponding to the above two postulates that provide a theoretical framework: What kind of effects and applications are predicted by macroscopic Maxwell's Equations, assuming no restrictions on $\varepsilon$ and $\mu$? How does one design and fabricate composites out of available materials to realize such unusual $\varepsilon$ and $\mu$?

A third, equally important question is whether one can observe the physical behavior of the composite predicted by EMT. In the case of conventional materials, the accuracy and generality of macroscopic Maxwell's Equations is confirmed by numerous experiments. For metamaterial composites, the applicability of EMT is, however, not fully established. To be able to predict the electromagnetic behavior of an arbitrary macroscopic composite based on its microscopic structure, considerable effort has been devoted to developing a general homogenization theory [5].

## 1. 3 History of Negative Refraction

In 1967, Veselago [6] considered materials with both $\varepsilon<0$ and $\mu<0$. Using macroscopic Maxwell Equations, he predicted that such a medium supports backward electromagnetic waves with opposite phase and group (energy) velocities. He also discussed several other unusual effects, such as reversed Doppler shift and Cerenkov radiation at an obtuse angle. Moreover, Veselago found that the refractive index should be $n=-\sqrt{\varepsilon\mu}$, which implies

that negative refraction occurs when light is incident on the interface between such a medium and air. Based on this effect, he further proposed that a flat slab composed of a medium with $\varepsilon=\mu=-1$(Fig. 1.1) acts as a lens, since it directs all the rays emitting from the object to the focus twice the lens thickness away.

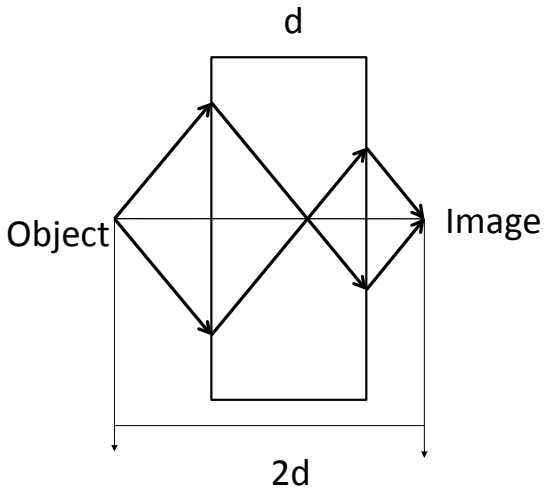


Fig. 1.1 A flat lens composed of an $\varepsilon=\mu=-1$ material. It forms an image by refocusing all the light rays emitting from an object through negative refraction.

Veselago was not the first to discuss backward wave or negative refraction [7]. H. Lamb [8] in 1904 and subsequently Pocklington [9] in 1905 discussed the existence of backward waves on certain mechanical systems. Almost at the same time, Schuster [10] considered backward waves and negative refraction in the context of electromagnetism.

Electromagnetic backward waves and negative refraction have since been studied by a number of authors. Mandel'shtam [11] in 1944 discussed negative refraction for media with opposite group and phase velocities. Malyuzhinets [12] in 1951 studied backward waves on radio-frequency transmission lines consisting of capacitors and inductors. Sivukhin [13] in 1957 was the first to consider materials with simultaneous negative $\varepsilon$ and

$\mu$, although he recognized that no such medium was known. Pafomov [14] further examined unusual Cerenkov effects in backward wave media.

Veselago was, however, the first to consider a negative refractive index and propose the flat lens in Fig. 1.1. Although he speculated about various physical systems that might be candidates to the hypothetical medium with simultaneous negative $\varepsilon$ and $\mu$, it was noted that no such material was known, and his theoretical consideration was on a "purely formal" basis [6]. For this reason, Veselago's work and the flat lens went largely unnoticed for nearly 30 years.

## 1. 4 Mesh Wires, Split Ring Resonators, and the Perfect Lens

Metals with good conductive properties have a negative $\varepsilon$ below the plasma frequency, which is typically in the ultraviolet region of the electromagnetic spectrum. The plasma frequency of the free electrons, $\omega_p$, is determined by the metal conduction electron density ($n$) through $\omega_p^2 = \frac{ne^2}{\varepsilon_0 m_{eff}}$, where $e$ is the electron charge, and $m_{eff}$ is its effective mass. For Al, $\omega_p$ is approximately 15eV. In 1996, Pendry [15] proposed that the artificial dielectric of conducting mesh wires [16, 17] may behave like a metal having a very diluted free electron density, with a plasma frequency in the microwave domain. Here we consider in Fig. 1.2 a simple 2D case of such a medium [18] with wires perpendicular to the diagram. The metallic wires are of radius $r$, and are placed periodically with spacing $a>>r$.

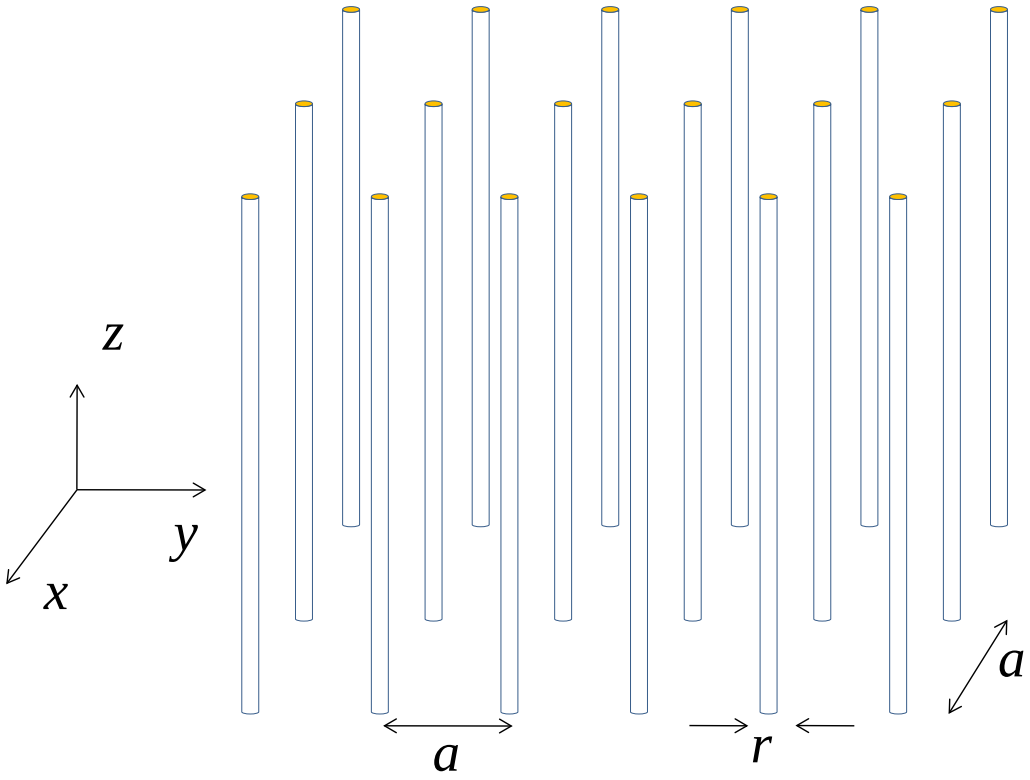


Fig. 1.2 A 2D wire medium where the infinitely long wires of radius *r* are along the *z* direction, and the square lattice spacing is *a*.

For transverse electric (TE, $\mathbf{E} = E\hat{\mathbf{z}}$) polarized electromagnetic waves, the electrons oscillating along *z* direction have a reduced effective density

$$n_{eff} = \frac{\pi r^2}{a^2} n . \tag{1.4}$$

Accounting for the self and mutual inductances due to the inhomogenous magnetic field and in the limit of $r -> 0$, the vector potential of the magnetic field at a distance *R* from a wire can be written as

$$\mathbf{A}(R) = \frac{\mu_0 \pi r^2 nev}{2\pi} \ln(a / R)\hat{\mathbf{z}} , \tag{1.5}$$

where $v$ is the mean electron drift velocity. An electron in a magnetic field corresponds to momentum $e\mathbf{A}$, which leads to an effective mass

$$m_{eff} = \frac{\mu_0 \pi r^2 n e^2}{2\pi} \ln(a/r), \tag{1.6}$$

assuming that electrons flow on the surface of the perfectly conducting metal wire. A typical set of parameters for the aluminum wire medium are $r$=1μm, $a$=5mm, and $n$=1.8×10$^{29}$ m$^{-3}$, which correspond to $m_{eff}$ =2.7×10$^4$$m_e$. The plasma frequency for the wire medium is therefore lowered to approximately 8.2 GHz due to the changes in $n_{eff}$ and $m_{eff}$. More detailed study of mesh wires can be found in Refs. [19-22].

In 1998, Pendry proposed split ring resonators (SRRs) [23, 24] as a means to achieve substantial magnetic response, and in particular negative $\mu$, in a desired frequency range [25]. Figure 1.3 shows the 2D case [18], where the metal rings with substantial self inductance are in the plane of the diagram and placed on a square lattice (not shown) of spacing $a$. In a transverse magnetic (TM, $\mathbf{H}=H\mathbf{z}$) polarized electromagnetic field, the large gaps in each ring force the current induced by the external varying magnetic field to complete the circuit through displacement currents flowing through the small radial gaps of width $d$ between the rings, which act as capacitors. Each pair of rings is therefore a resonant L–C (inductor-capacitor) circuit, which results in a dispersive magnetic response. The effective permeability is given by the ratio of average B to H fields, that is, $\mu_{eff} = \frac{B_{ave}}{H_{ave}}$. Assuming that the capacitance due to the large gaps in a single ring is negligible, and the wire and small gap widths are both also small compared to the ring

radius of $r$, a procedure [26] that calculates the average fields by their line or surface averages gives:

$$\mu_{eff} = 1 - \frac{f\omega^2}{\omega_0^2 - \omega^2} \tag{1.7}$$

as a function of frequency, where the resonant frequency $\omega_0 = (\frac{3d}{\mu_0 \varepsilon_0 \pi^2 r^3})^{1/2}$, and filling factor $f = \pi r^2 / a^2$. $\mu_{eff}$ is negative between $\omega_0$ and the "magnetic plasma frequency" of $\omega_m = \left( \frac{3d}{(1-f)\mu_0 \varepsilon_0 \pi^2 r^3} \right)^{1/2}$. For a set of typical parameters of $r$=1.5mm, $a$=5mm, $d$=0.2mm, these frequencies are $\omega_0$ =6.41GHz, $\omega_m$ =7.56GHz. Note that the bandwidth with a negative $\mu$ can be tuned by $d$ and $f$.

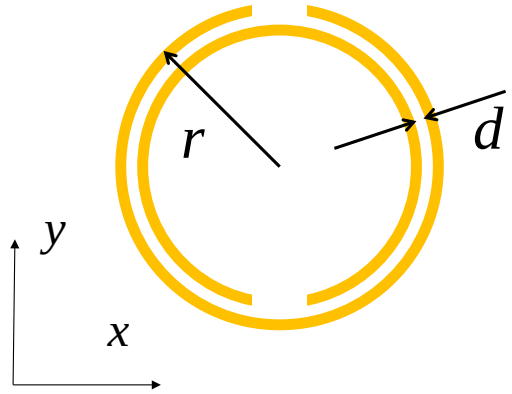


Fig. 1.3 A pair of split ring resonators as an L-C circuit. The rings are of radius $r$, and the radial gap is of width $d << r$.

In 2000, Pendry published the seminal paper titled "Negative Refraction Makes a Perfect Lens" [27]. He considered isotropic materials with $\varepsilon$ and $\mu$ <0, and used Fresnel's

formula to calculate the transmission of plane waves through the flat lens in Fig. 1.1. When both $\varepsilon$ and $\mu$ approach -1, the surprising result is that the limit of transmission is unity, independent of the transverse wavevector of the incident radiation. This result suggests that such a slab would result in a perfect image of a point light source, since it would restore all Fourier components of the optical field of an object, including evanescent waves. The flat lens made of $\varepsilon=\mu=-1$ materials (the Veselago-Pendry lens) hence promises a superior optical imaging device based on negative refraction, and is therefore named the "perfect lens" or "superlens". Although Pendry recognized the lack of such materials, he proposed that they may be engineered from known composites with negative $\varepsilon$ and $\mu$, such as mesh wires and SRRs. The perfect lens paper ignited the field of metamaterials, which has since seen thousands of academic publications in the ensuing decade [18, 28-34].

## 1. 5 Transformation Optics and Invisibility Cloaking

Based on the invariance of macroscopic Maxwell's Equations under coordinate transformation, Pendry *et al* [35] in 2006 further proposed optical devices using anisotropic metamaterials with spatially dependent $\varepsilon$ and $\mu$ tensors. A similar scheme based on conformal mapping in the geometrical optics formulation was developed at the same time by Leonhardt [36].

Under a coordinate transformation, macroscopic Maxwell Equations and constitutive relations maintain the same form, provided the material parameters and fields in the new coordinate system are transformed and scaled accordingly. For example, when the

transformation maps Cartesian coordinates ($x$, $y$, $z$) to another system of orthogonal coordinates ($u$, $v$, $w$), the corresponding scaling is [35]:

$$\begin{aligned} \varepsilon_i' &= \varepsilon_i \frac{Q_u Q_v Q_w}{Q_i^2} \\ \mu_i' &= \mu_i \frac{Q_u Q_v Q_w}{Q_i^2} \\ E_i' &= Q_i E_i \\ H_i' &= Q_i H_i \end{aligned} \tag{1.8}$$

Here, quantities with a prime are those after scaling, $i$ is a subscript used to denote field or tensor components in the $u$, $v$, or $w$ directions (with no index contraction), and $Q_i$'s are given by:

$$\begin{aligned} Q_u^2 &= (\frac{\partial x}{\partial u})^2 + (\frac{\partial y}{\partial u})^2 + (\frac{\partial z}{\partial u})^2 \\ Q_v^2 &= (\frac{\partial x}{\partial v})^2 + (\frac{\partial y}{\partial v})^2 + (\frac{\partial z}{\partial v})^2 \\ Q_w^2 &= (\frac{\partial x}{\partial w})^2 + (\frac{\partial y}{\partial w})^2 + (\frac{\partial z}{\partial w})^2 \end{aligned} \quad . \tag{1.9}$$

Transformation to non-orthogonal coordinates results in more complicated, but similar expressions.

This formalism, now known as "transformation optics" [33], allows the solution of "invisibility cloaking" problem within EMT, as shown in Fig. 1.4(a), where any light ray (yellow line) incident on the blue outer sphere is required to be bent smoothly around the red inner sphere without scattering, thereby maintains its propagation direction to exit the blue sphere. Thus an observer outside the outer sphere will not detect any object within the inner sphere. Consider a coordinate transformation that expands the shell region between the spheres (the "cloak") in Fig. 1.4(a) to the entire blue sphere in Fig. 1.4(b). The invariance of macroscopic Maxwell Equations allows considering the same

electromagnetic problem, formulated in the new coordinate system with scaled fields and material parameters, in the virtual space of Fig. 1.4(b). Since the inner sphere has been

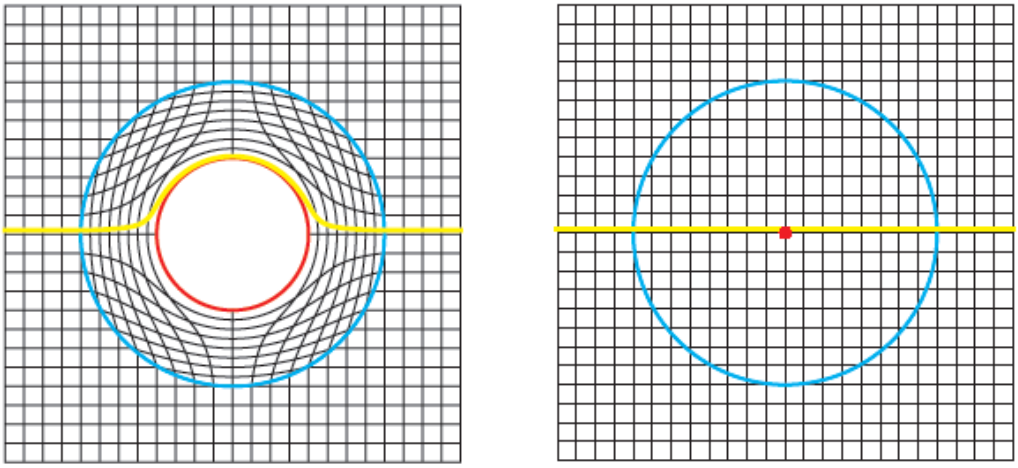


Fig. 1.4 (a) Real space with warped phase fronts. (b) Virtual space with parallel phase fronts. Reprinted from Ref. [33] with permission from Macmillan Publishers Ltd.

reduced to a point, the cloaking requirement of the shell (the entire blue sphere in the virtual space) is satisfied by a homogeneous isotropic medium with $\varepsilon'=\mu'=1$ for any incident field. An inverse transformation of these parameters back to the real space in Fig. 1.4(a) therefore yields the required distribution of $\varepsilon$ and $\mu$ tensors. Since this transformation of material parameters is determined only by the coordinate transformation, the cloaking requirement is also satisfied for an *arbitrary* incident field in real space.

## 1. 6 Prior Experimental Demonstrations of Metamaterials

In 2000, Smith *et al.* [37] fabricated a periodic metal dielectric composite consisting of wires and SRRs, and observed transmission consistent with a homogeneous medium with simultaneously negative $\varepsilon$ and $\mu$ at microwave frequencies. In a subsequent experiment [38], a right-angled prism (Fig. 1.5(a)) composed of a similar composite was mounted in the experimental setup shown in Fig. 1.5(b), where the incident electromagnetic wave was normally incident on the bottom of the prism from a waveguide, and refracted at its hypotenuse. The refractive index was determined using Snell's law from the detected direction of the outgoing beam and was shown to be negative. The observed negative index was also fit to a model of dispersive negative $\varepsilon$ and $\mu$. These composites are now known as negative index metamaterials (NIMs).

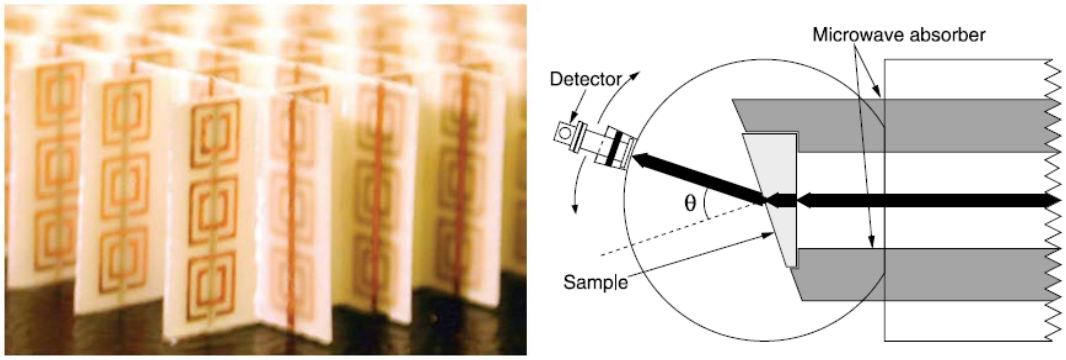


(a) (b)

Fig. 1.5 (a) The negative index metamaterial (NIM) prism. (b) Schematic of the experimental setup. Reprinted from Ref. [38] with permission from AAAS.

Controversies, however, ensued on the interpretation of this experiment, in particular on the strong absorption [39] by the NIM and the possible near-field effect due to the proximity of the detector to the prism [40]. The physical effect of negative refraction was nevertheless confirmed by similar prism experiments [41, 42], where the measurement was performed in the far field on less lossy NIMs. These experiments were considered decisive evidence for the existence of materials with negative $\varepsilon$ and $\mu$ [43].

Negative refraction has also been observed in periodic dielectric photonic crystals [44]. Although there is not a clear distinction between the two types of periodic structures, it is common to differentiate them conceptually [28, 38]: negative refraction by photonic crystals is due to Bragg diffraction, whereas NIMs are effective media.

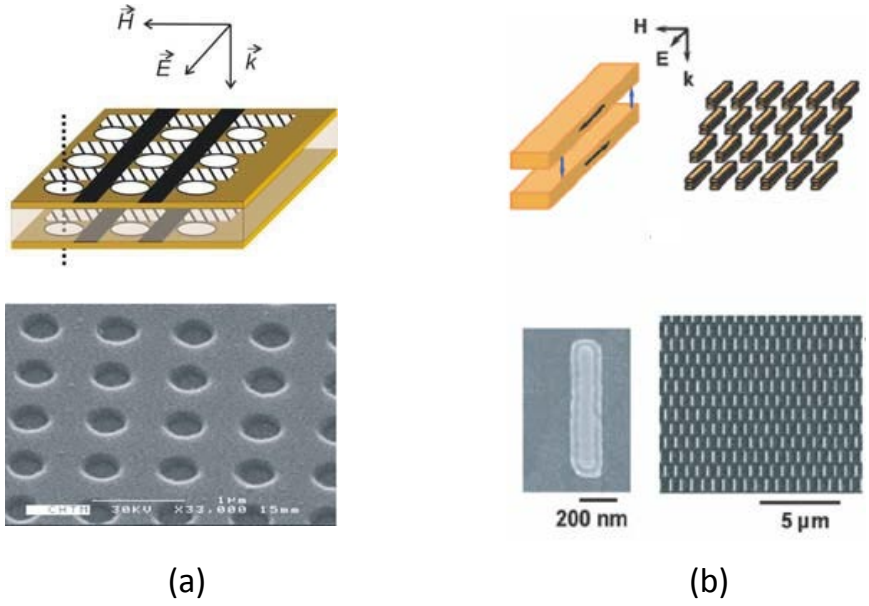


Fig. 1.6 Schematics and electron micrographs of near-infrared NIM structures. (a) A double fishnet. Reprinted from Ref. [45] with permission from the American Physical Society. (b) Coupled nanorods. Reprinted from Ref. [46] with permission from the Optical Society of America.

In 2005, two metal dielectric NIM structures operating at near infrared frequencies were fabricated: a double fishnet (Fig. 1.6(a)) [45] and coupled nanorods (Fig. 1.6(b)) [46]. Direct [46] or indirect [45] phase measurements indicate negative phase advance through a single layer of these structures at the wavelength of $\lambda$=1.5μm and 2μm, respectively. These NIMs, however, have at least one dimension that is approaching half of the operating wavelength.

In 2006, the first two-dimensional cloaking device consisting of spatially varying magnetic metamaterial unit cells (Fig. 1.7(a)) was fabricated [47]. It was used to partly conceal a copper cylinder placed at its center in a microwave scattering experiment. Fig. 1.7(b) shows the EMT predicted scattering pattern, while the experimentally measured field map is shown in Fig. 1.7(c). Recent literature on cloaking can be found in Ref. [33].

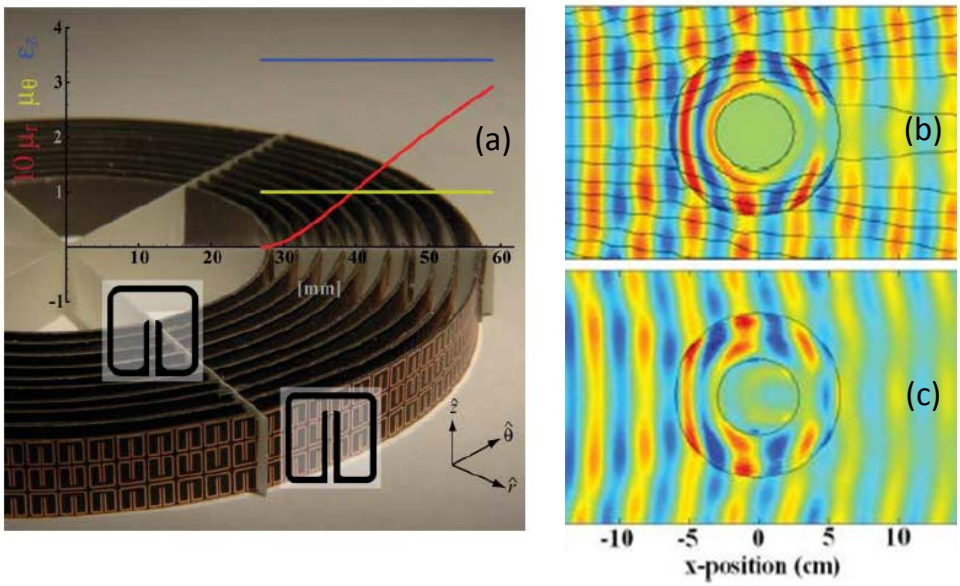


Fig. 1.7 (a) An electromagnetic cloak consisting of spatially varying magnetic metamaterial unit cells. (b) EMT predicted scattering pattern. (c) Experimental mapping of the electric field. Reprinted from Ref. [47] with permission from AAAS.

## 1. 7 Outstanding Questions and Thesis Overview

Although there has been an enormous volume of prior work [18, 28-31], the following questions on NIMs are left outstanding:

1. What is the refractive index of an arbitrary NIM?

2. What is the maximum unit cell size for a NIM?

3. Is there a fundamental difference between NIMs and photonic crystals that exhibit negative refraction?

4. Is it possible to engineer an optical NIM with a subwavelength periodicity?

5. Can the concept of a “perfect lens” be theoretically justified?

This dissertation aims to answer these questions with an emphasis on the physical behavior of NIMs. Since almost all NIMs in the literature are periodic, and aperiodic NIMs are unlikely to provide advantage in fabrication or performance, we focus here on periodic NIMs. In Chapter 2, we first derive a maximum unit cell size and a general relationship between the bulk negative index of an arbitrary NIM and its photonic band structure in the zero-loss limit. This is extended to the case of finite loss based on a generalized phase matching condition, and we provide a unified explanation of negative refraction observed in both lossless photonic crystals and lossy metal-dielectric NIMs. In Chapter 3, a subwavelength near-infrared NIM is fabricated using electron beam lithography, and its dimensions are characterized. A negative phase advance through this NIM is also observed through interferometry, and compared with its bulk negative index. In Chapter 4, a model NIM based on Mie resonances in cylinders with positive $\varepsilon$ and $\mu$ is

designed. After homogenization, we show that the material exhibits $\varepsilon=\mu=-1$. EMT is found to significantly overestimate the range of evanescent waves that can be recovered by a flat NIM lens due to neglect of its microstructure. The implications of this result on constructing a perfect lens are discussed, and the necessity for using microscopic models is emphasized. In Chapter 5, we summarize the results. Chapter 2 has been published in Refs. [48, 49], Chapter 3 has been published in Refs. [50-52], and Chapter 4 has been submitted for publication [53] ().

# CHAPTER 2

## Photonic Band Theory of Negative Index Metamaterials

The standard model for describing negative index metamaterials (NIMs) is effective medium theory (EMT). For example, the refractive indices of NIMs operating at near-infrared or higher optical frequencies [31] have been typically characterized using a homogenization approach, such as the scattering (*S*) parameter method [54]. By assuming that the NIM slab, actually composed of discrete elements, is equivalent to a homogeneous NIM, the *S*-parameter method calculates the permittivity, $\varepsilon$, and permeability, $\mu$, from its complex transmittance and reflectance, and the refractive index is obtained as $n = -\sqrt{\varepsilon\mu}$. However, the *S*-parameter method is known to yield anomalies such as non-physical negative imaginary parts of $\varepsilon$ or $\mu$ [55]. In addition, the assumption of a homogeneous medium is questionable, especially in the optical domain, since optical NIMs thus far involve unit cell sizes close to half of the wavelength in at least one dimension [56]. Moreover, a negative refractive index should be a bulk property and consistent with Snell's Law. The negative index obtained with the *S*-parameter method may change with an increasing number of layers of NIM unit cells [57] and in

particular, may reverse its sign [58]. This index also lacks the physical meaning of refraction [59] if it is not verified by Snell's Law. With the possible exception of work on surface plasmon polaritons in a waveguide [60], to our knowledge no refraction experiment or rigorous first-principles calculations on a fabricated structure has confirmed the existence of a negative refractive index for bulk optical metamaterials.

At microwave frequencies, however, negative refraction has been observed in two experiments [41, 61], which are considered evidence of NIMs [43]. These experiments employ prisms composed of one-dimensional (1D) NIM unit cells that exhibit a negative phase index in a particular direction. In those experiments, the incident electromagnetic wave propagates within the prism along this direction, such that anisotropy of the unit cell does not play a role. The electromagnetic wave is obliquely incident on the hypotenuse from within the prism, and the refracted beam is detected in the far field. Negative refraction occurs due to the negative phase index, i.e. anti-parallel energy velocity and wave vector, rather than anisotropy of the material, accompanied by a positive phase index [62]. In Ref. [41], the index determined by the *S*-parameter method was shown to agree with Snell's Law. In Ref. [61], refractive indices measured on two different prisms (i.e. at two different incidence angles) consisting of the same unit cells were shown to be equal.

In this chapter, we use photonic band theory for periodic composites to predict the bulk refractive index of NIMs, and describe their negative refraction as diffraction at a periodic boundary. We introduce a near-infrared NIM structure with a subwavelength periodicity. Using this NIM structure as a prototype, we derive in the zero-loss limit a general relationship between the band structure of an *arbitrary* NIM unit cell and its bulk

refractive index. In addition, we determine the maximum unit cell size that defines the "metamaterial regime" [D. R. Smith *et al.*, Phys. Rev. E, **71**, 036617 (2005)]. Finally, using a generalized phase matching condition for the case of finite loss, we provide a unified explanation of negative refraction observed in both lossless photonic crystals and lossy metal-dielectric NIMs.

## 2. 1 Bulk Negative Index of a Subwavelength Near-Infrared NIM

The NIM unit cell is shown in the inset of Fig. 2.1(a). It consists of 20-nm thick by 100-nm wide Au strips, separated from a 20-nm thick central continuous Au layer [63] by 15-nm thick polymer dielectric spacers. The unit cell extends infinitely along the $\hat{z}$ direction, and is replicated in both the $\hat{x}$ and $\hat{y}$ directions with a period of 150 nm. These dimensions are consistent with a fabricated structure [50] that will be described in Chapter 3. For transverse magnetic (TM)-polarized electromagnetic wave propagating along $\hat{x}$ in the *x*-*y* plane, i.e., $\mathbf{H}=H_z\hat{z}$, the unit cell is a resonator supporting even- and odd-$H_z$ modes with respect to the central plane. Currents flow in opposite (same) directions along the strips in even (odd) resonance, which is associated with an magnetic (electric) dipole response that is weakly (strongly) dependent on the presence of the central metallic layer [63].

Normal incidence plane wave scattering simulations are performed on a single layer of unit cells to calculate the effective refractive index with the *S*-parameter method [54]. The refractive index of the polymer dielectric is $n_d = 1.56$ (corresponding to that of

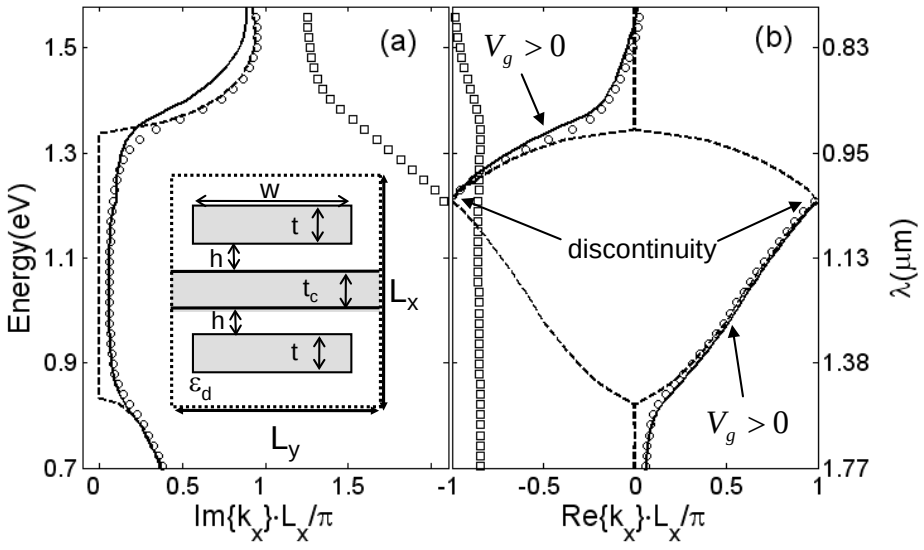


Fig. 2.1 Bloch bands for zero (dashes) and non-zero dissipation (circles and squares) Au layers, and (a) imaginary and (b) real parts of the effective propagation constant $k_{x,eff}$ from single-layer scattering simulations (continuous line). In (b), the part of lossless band structure with a positive group velocity $v_g > 0$ is marked by arrows. Inset in (a): the unit cell. Lattice constants $L_x = L_y =$ 150nm, Au strip and central layer thicknesses $t=t_c=20$nm, strip width W=100nm, and spacer thickness h=15nm. Au strips and central layer are embedded in a polymer dielectric.

cyclotene), and dielectric constants of Au are taken from the literature [64]. The index is converted to an effective propagation constant using $k_{x,eff} = n_{x,eff} \cdot \omega / c = n_{x,eff} \cdot k_0$, and is plotted in Figs. 2.1(a) and (b). Here, $\omega$ is the angular frequency, $c$ is the speed of light, and $k_0$ is the wave number in free space. These propagation constants coincide with those derived from Bloch-band calculations (circles and squares) within the first Brillouin zone [65]. Despite the existence of two bands within the same wavelength range, only the least lossy mode (circles, with the smallest Im($k_x$)) participates in light propagation in the crystal [66]. This coincidence shows that for a beam traversing a slab containing a

sufficiently large number of layers of the structure, the phase delay due to the slab thickness of $d$ can be asymptotically written as $\mathrm{Re}(k_{x,eff})d = \mathrm{Re}(n_{x,eff})k_0 d$, since phase changes due to the surfaces and possible truncation of the surface unit cells are bounded and hence can be omitted, and multiple reflection amplitudes are negligibly small for any finite $\mathrm{Im}(k_{x,eff})$. This index is independent of $d$, and is therefore indeed a bulk property. It will be further validated in Sec. 2.2 through its consistency with Snell's Law.

The Bloch band diagram for the unit cell assuming lossless Au (i.e. with zero imaginary permittivity) is also plotted in Figs. 2.1(a) and (b) as dashed lines. The band shown by squares has even less contribution to light propagation than in the lossy case due to its large imaginary part, and is therefore omitted. The Bloch wavevector is real between $\lambda$=0.93 and 1.5 μm, a range in which the dimensions of the unit cell are subwavelength (~$\lambda$/7). Note that this hypothetical NIM possesses both positive and negative index bands.

## 2. 2 Refractive Index and Maximum Unit Cell Size in Zero-Loss Limit

### 2. 2. 1 General Relationship between Effective Index and Band Structure

In Fig. 2.1(b), the discontinuity in $\mathrm{Re}(k_{x,eff})$ at $\lambda \approx 1\mu m$ leads to a discontinuity in $\mathrm{Re}(n_{x,eff})$. The negative and positive index bands separated by this discontinuity correspond to negative and positive refraction, respectively [41, 61]. Consider a two-dimensional semi-infinite metamaterial crystal in the *x*-*y* plane composed of these unit cells, as shown in Fig. 2.2(a). The unit cells are made from dielectric and lossless metal,

such that the energy and group velocities of propagating Bloch modes are equal [67]. Furthermore, we assume a TM polarized Bloch mode propagating along $\hat{x}$, with wavevector $\vec{k}$ in the first Brillouin zone obliquely incident at the metamaterial-air interface. These modes therefore correspond to the region of the dispersion curves with a positive group velocity, as shown in Fig. 2.1(b). Due to the finite size of the unit cell, the metamaterial-air interface is stepped, with angle $\theta = \arcsin(a/d) = \arcsin(1/\sqrt{1+m^2})$.

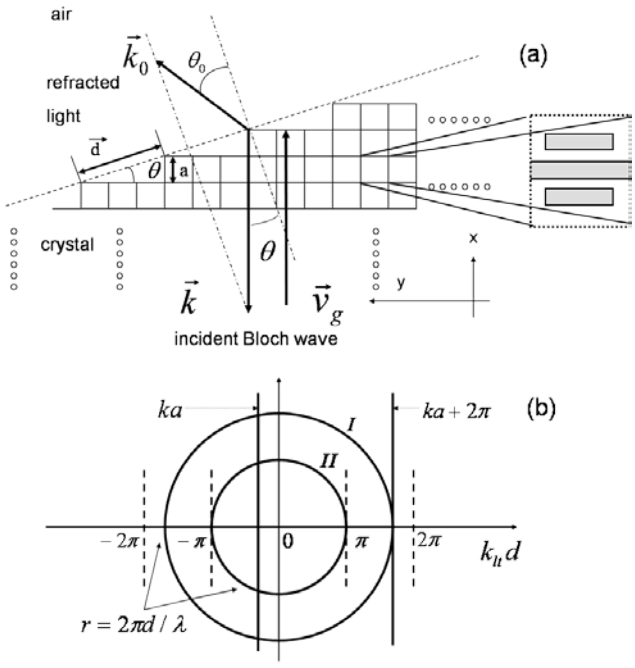


Fig. 2.2 (a) A Bloch wave propagates in the positive $\hat{x}$ direction and is obliquely incident upon the semi-infinite metamaterial crystal's interface with air. Only a small number of unit cells near the interface are shown. Here, *a* is the lattice constant, *d* is the interface periodicity. $\vec{k}$ and $\vec{v}_g$ are first Brillouin zone wavevector and group velocity of the incident Bloch wave. $\vec{k}_0$ is the free space wavevector of the refracted light. $\theta$ and $\theta_0$ are incidence and refraction angles, respectively. (b) Graphical solutions to $ka + l \cdot 2\pi = k_{lt}d$. Radii of circles I and II are $ka + 2\pi$ (for $-\pi < ka < 0$) and $\pi$, respectively.

Here $a$ is the NIM lattice constant, $d = \sqrt{1+m^2}\,a$ is the interface periodicity, and there are one and $m$ unit cells along $\hat{x}$ and $\hat{y}$ per step, respectively, as previously [41, 61, 68]. The resulting interface grating diffracts the incident Bloch wave into the transmitted waves.

Far from the interface the scattered optical field can be written as a sum of plane waves following $H(\vec{r}) = \sum_l a_l \exp(i\vec{k}_l \cdot \vec{r})$, where $H$ is the magnetic field, $\vec{k}_l$ is the free space wavevector ($|k_l| = 2\pi/\lambda$), and $a_l$ is the coefficient for the $l^{\text{th}}$ term. The component of $\vec{k}_l$ parallel to the interface is related to that of the incident Bloch wavevector, $\vec{k}$, through

$$k_{lt} = k_t + l \cdot G, \tag{2.1}$$

where $k_t = k\sin\theta$, and $G = 2\pi/d$ is the magnitude of the surface reciprocal lattice vector. When $l$=0, $k_{0t} = k_0 \sin\theta_0 = k\sin\theta$, which is equivalent to Snell's Law, $\sin\theta_0 = n_{eff}\sin\theta$, where $\theta_0$ is the refraction angle. The effective refractive index of the metamaterial is therefore related to the Bloch wavevector via $n_{eff} = k/k_0$, independent of the incidence angle $\theta$ (or $m$), as in Ref. [61]. This also shows that higher orders that correspond to non-zero $l$ do not give rise to an effective index that satisfies such a condition. Accounting for both positive and negative index bands, the effective index can be written as

$$n_{eff} = v_g k / |v_g| k_0 = (k/k_0)\,\mathrm{sgn}(v_g) = (k/k_0)\,\mathrm{sgn}\left(\frac{\partial\omega}{\partial\,\mathrm{Re}(k)}\right) \tag{2.2}$$

Fig. 2.1(b) therefore shows that a sufficiently large prism consisting of our (lossless) NIM will undergo negative refraction in the negative index band of 0.93μm < λ < 1.03μm.

Equation 2.2 connects the first Brillouin-zone band structure of a 1D lossless subwavelength unit cell to its effective index exhibited in a prism refraction experiment. Although its derivation is for TM polarization and the unit cell of Fig. 2.1(a), we emphasize that it is *general* since it utilizes only the discrete translational symmetry along the metamaterial-air interface. The generalization of the analysis to arbitrary polarization and a 3D subwavelength unit cell is straightforward provided that it has a dominant Bloch band in the incidence direction.

### 2. 2. 2 Maximum Unit Cell Size

Equation 2.1 is equivalent to $ka + l \cdot 2\pi = k_{lt} d$, with graphical solutions shown in Fig. 2.2(b). Each solution of $k_{lt}$ represents a propagating order in the air. In Sec. 2.2.1, we have shown that the $0^{th}$ order corresponds to experimentally observed negative refraction, with a negative refractive index that is independent of the incidence angle $\theta$ or $m$. For well-defined negative refraction to occur, however, there must be at most one far-field beam. Higher orders in Eq. 2.1 that correspond to non-zero $l$ must therefore be absent in the far field. Inspection of Fig. 2.2(b) shows for $-\pi < ka < 0$, the maximum $d$ that satisfies this condition is given by the radius of circle I, or $d_c = \lambda(1 + ka/2\pi) < \lambda$, which also restricts $m$ and $\theta$ to those allowed by $d<d_c$. Circle II indicates that $d < d_s = \lambda_{\min}/2$

constitutes a sufficient condition across the entire negative index band, of which $\lambda_{min}$ is the minimum wavelength.

The justification for applying effective medium theory to metamaterials in the literature is that the unit cell size is much smaller than the wavelength. However, for most NIMs fabricated to date, typically $\lambda / a < 12$ [56]. At the same time, while effective medium theory only applies in the limit of $ka \to 0$, for practical metamaterials $|ka| \sim 1$, a scale that Smith, *et al.* refer to as the "metamaterial regime" [69]. Hence, $d_c$ and $d_s$ are quantitative limits that define such a metamaterial regime for NIMs in refraction experiments based on physical equivalence. These limits and Eq. 2.2 serve as criteria for the design of NIM unit cells.

### 2. 2. 3 Numerical Simulation of Prism Refraction

A practical structure must be low-loss, for which the above results are also expected to apply. Indeed, the small differences in Figs. 2.1(a) and (b) between the band structure of the lossless and the realistic NIM imply that Eq. 2.2 is still true for the latter. To confirm this, we performed full-wave simulations of wedges composed of the unit cells in Fig. 2.1(a), with the bottom illuminated by a normally incident TM plane wave. The main lobe of the time-averaged power flow of the transmitted wave determines the direction of the refracted beam, which is used to calculate the effective refractive index based on Snell's law. Wedges defined by $m$=2 and 3 were simulated, corresponding to incidence angles of $26^o$ and $18^o$, respectively, as in Ref [61], which also used square unit cells. Both

geometries satisfy the condition that $d<d_c$ throughout the simulated frequency range. A representative field plot on the logarithmic scale is shown in the inset of Fig. 2.3. In the negative index band, refraction and diffraction coexist, consistent with experiments in the microwave domain [68]. We will explain the diffracted beam almost bound to the hypotenuse with full account of loss in Sec. 2.3. Apart from the main lobe, in most situations two weak side lobes are also apparent. The width of the illuminated part is four steps for both $m$=2 and 3 wedges, suggesting that the weak side lobes are similar to secondary maxima observed in multiple-slit diffraction experiments. Both features were also observed in microwave frequency simulations of a homogeneous NIM prism [68]. A sufficiently large prism eliminates side lobes, and the refracted beam would emerge uniformly along the hypotenuse.

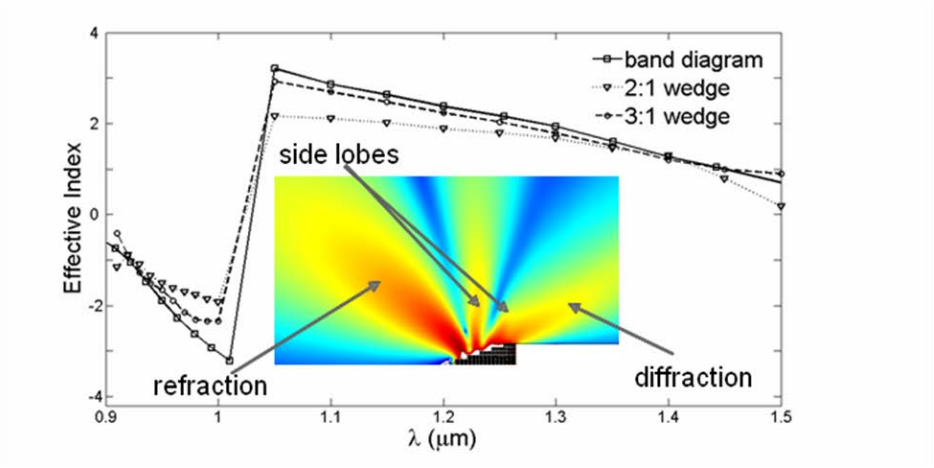


Fig. 2.3 Comparison of effective indices extracted from numerical simulations and band calculations. Inset: Time averaged power flow on the logarithmic scale for an $m$=3 wedge at wavelength $\lambda$=950nm. A negatively refracted beam, a diffraction order, and two weak side lobes are observed.

Between $\lambda$=0.91$\mu$m and 1.5$\mu$m, refractive indices extracted from the full-wave simulations and band structure are plotted in Fig. 2.3, which are consistent with each other. The saturation of the $m$=2 wedge index (triangles) at $n=\pm 2$ for 0.96$\mu$m < $\lambda$ < 1.2$\mu$m results since the Bloch-band derived index in this range exceeds the condition for total internal reflection defined by $|n_{\max}|$ =1/sin(26$^o$)=2.2. Note that in a recently published refraction experiment [70] using the fishnet structure at a wavelength of 1.5$\mu$m, the relation between the band structure and the measured effective index is also consistent with Eq. 2.2.

### 2. 2. 4 Role of Transverse Unit Cell Size

A homogeneous NIM prism gives rise to no more than one propagating order in air at all incidence angles. To justify the characterization of a NIM structure with a negative index, the refractive behavior of a composite NIM prism made of such unit cells should be consistent with that of a homogeneous NIM prism within the negative index band in an incidence angle range as large as possible, which was shown to be limited by $d_c$ and $d_s$. Optical NIMs demonstrated to date typically have lateral dimensions close to $\lambda$/2 [31]. In particular, the lateral unit cell sizes for fishnet structures are constrained by its high magnetic resonance frequency [56, 71]. The longitudinal period of a fishnet structure can be very small compared to $\lambda$ [57], and the incidence angle can be varied almost continuously by changing the number of unit cells in this direction. However,

given that the negative index is necessarily strongly dispersive and $|ka|$ is often on the order of unity [69], the maximum incidence angle for a fishnet structure is restricted by its large transverse dimensions. Our unit cell has a much more subwavelength size in the transverse direction, and this restriction is therefore considerably loosened.

## 2. 3 Generalized Phase Matching Condition with Finite Loss

In Sec. 2.2, we used Eq. 2.1 to consider diffraction of a real Bloch wave by the prism hypotenuse in the zero-loss limit, and derived a general relation (Eq. 2.2) between the effective index and real band structure. Equation 2.1 is the scalar form of a phase matching condition across an interface of periodicity *d*, $\mathbf{k}_t^{\mathrm{B}} = \mathbf{k}_t^m + m\mathbf{G}$ . Here, $|\mathbf{G}| = 2\pi / \mathrm{d}$ is the magnitude of the interface reciprocal lattice vector, *m* is an integer for denoting different diffraction orders, and $\mathbf{k}^{\mathrm{B}}$ and $\mathbf{k}^m$ are *real* wave vectors of a Bloch and a plane wave, respectively. This phase matching condition is a corollary of Bloch's Theorem [72], and connects the transverse components (denoted by subscript, *t*) of $\mathbf{k}^{\mathrm{B}}$ and $\mathbf{k}^m$. It has also been used for describing the diffraction of quantum mechanical Bloch waves into free space in angle resolved photoemission spectroscopy experiments [73] that probe the electronic band structure of a solid.

We applied Eq. 2.2 approximately to the full complex band structure of the NIM unit cell in Sec. 2.1, and achieved reasonable agreement between the effective index and full-wave simulations of prism refraction (Fig. 2.3). However, substantial differences persist,

particularly near the boundary of the Brillouin zone. The appearance of the nearly grazing beam in Fig. 2.3 was also not explained. In addition, derivation of Eq. 2.1 implicitly assumes that the Bloch wave vector is either parallel or anti-parallel to the group velocity, which is not necessarily true in the more general case of unit cells with anisotropy [74]. Moreover, it is not clear whether the neglect of loss is always justified. Indeed, the issue of how lossy materials might influence experimental interpretation has been controversial [39] since the first demonstration of negative refraction by NIMs at microwave frequencies [38].

The deviations in Fig. 2.3 may be due to neglect of losses. To extend Eq. 2.2 to the more general case of lossy periodic media, one needs to account for the *imaginary* component of the wave vector. Although complex band structure of metamaterials has been routinely calculated, refraction experiments [38, 41, 42] that demonstrate negative refraction by NIM prisms are interpreted using EMT. To our knowledge, diffraction of complex Bloch waves by periodic photonic structures has not been generally treated.

In this section, we generalize treatment of NIM refraction in Sec. 2.2 by including the effect of losses and possible anisotropy. Based on a generalized phase matching condition with a complex transverse wave vector for periodic media, we describe the diffraction of a complex Bloch wave propagating within a composite prism, and show that the detected light is an inhomogeneous plane wave due to losses in the prism.

### 2. 3. 1 Diffraction of a Complex Bloch Wave

Figure 2.4 shows a schematic of a NIM negative refraction experiment, which is similar to Fig. 2.2(a) but takes loss into account. A plane wave is normally incident along $\hat{\mathbf{x}}'$ on the

bottom of the prism composed of cubic unit cells of size *a*, and excites complex Bloch modes within the prsim, where $\hat{\mathbf{z}}$ is normal to the plane of incidence. We assume a sufficiently large but finite prism, such that multiple reflections within the prism and diffraction by its corners can be neglected. The wave vector of the Bloch mode in the first Brillouin zone must be along $\hat{\mathbf{x}}'$, due to conservation of its transverse component. The complex dispersion

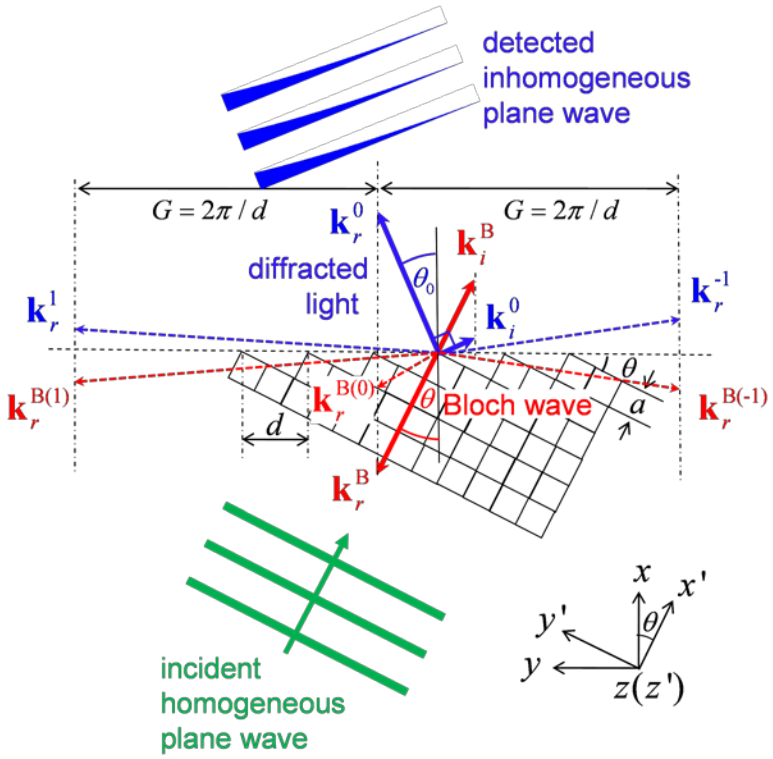


Fig. 2.4. A homogeneous plane wave is normally incident along $\hat{\mathbf{x}}'$ in the *x'-y'* plane on a composite prism consisting of subwavelength unit cells and excites a complex Bloch wave that is diffracted by the interface grating at the hypotenuse. The diffracted light is detected in the far field. Constant and exponentially decaying wave amplitudes of phase fronts represent the incident homogeneous and detected inhomogeneous plane waves, respectively. Here, $\theta$ and $\theta_0$ are incidence and refraction angles, $a$ is the unit cell size, $d$ is the interface periodicity, $\mathbf{k}^B$ is the first Brillouin zone wave vector of the Bloch mode, and $\mathbf{k}^m$ and $\mathbf{k}^{B(m)}$ are the complex wave vector of the $m^{th}$ transmitted diffraction order and reflected Bloch wave in the extended Brillouin zone scheme, respectively. Subscripts $r$ and $i$ denote real and imaginary parts, and $G = 2\pi / d$ is the magnitude of the surface reciprocal lattice vector.

relation of this Bloch mode, $k^{\mathrm{B}} = k^{\mathrm{B}}(\omega)$, can be calculated [75]. Here, $\omega$ is the (real) angular frequency, $k_r^{\mathrm{B}} = \mathrm{Re}(k^{\mathrm{B}})$, and $k_i^{\mathrm{B}} = \mathrm{Im}(k^{\mathrm{B}})$. This choice of real frequency and complex wave vector is consistent with typical experiments that are conducted in the frequency domain with near monochromatic illumination [41]. The electric and magnetic field of this Bloch mode are $\mathbf{E}(\mathbf{r}') = \mathbf{E}_0(\mathbf{r}')\exp(ik_r^{\mathrm{B}}x' - k_i^{\mathrm{B}}x')$ and $\mathbf{H}(\mathbf{r}') = \mathbf{H}_0(\mathbf{r}')\exp(ik_r^{\mathrm{B}}x' - k_i^{\mathrm{B}}x')$, respectively. Here, $\mathbf{r}' = (x', y', z')$, and $\mathbf{E}_0(\mathbf{r}')$ and $\mathbf{H}_0(\mathbf{r}')$ are both functions periodic on the cubic lattice. The $x'$ component of the time averaged power flow of this Bloch mode per unit cell is given by the surface integral of the Poynting vector $\mathbf{E}_0(\mathbf{r}') \times \mathbf{H}_0^{*}(\mathbf{r}')$ (proportional to momentum density), i.e.,

$$\begin{aligned} P(x') &= \frac{1}{2}\mathrm{Re}\Big( \int_{S(x')} (\mathbf{E}(\mathbf{r}') \times \mathbf{H}^{*}(\mathbf{r}')) \cdot \hat{\mathbf{x}}' dy' dz' \Big) \\ &= \frac{1}{2}\mathrm{Re}\Big( \int_{S(x')} (\mathbf{E}_0(\mathbf{r}') \times \mathbf{H}_0^{*}(\mathbf{r}')) \cdot \hat{\mathbf{x}}' \, \mathrm{e}^{-2k_i^{\mathrm{B}}x'} \, dy' dz' \Big) \end{aligned}, \tag{2.3}$$

where $S(x')$ is the cross section of a *single* unit cell at $x'$ in the $y' - z'$ plane. Therefore, $P(x' + a) = P(x')\exp(-2k_i^{\mathrm{B}}a)$, and has no $y'$ or $z'$ dependence, due to the periodicity of $\mathbf{E}_0(\mathbf{r}')$ and $\mathbf{H}_0(\mathbf{r}')$. Since power must flow away from the surface, $k_i^{\mathrm{B}} > 0$, corresponding to decay of $P(x')$ along $\hat{\mathbf{x}}'$ due to dissipation within the composite, although in general the local Poynting vector and wave vector may not be in the same direction [76]. Similar considerations of $y'$ and $z'$ components of the power flow per unit cell show that they are periodic, but do not decay, along their respective axes. These components are not necessarily zero, due to the possible anisotropy of the unit cell [74].

Therefore, we do not assume a total power flow along $\hat{\mathbf{x}}'$, although typical unit cells [38, 41, 42] are, by design, approximately symmetric with respect to the $z'-x'$ plane.

For a sufficiently large prism, only the complex Bloch mode with the lowest loss (corresponding to the smallest positive $k_i^{\mathrm{B}}$) contributes to wave propagation within the bulk of the composite [66, 77]. Modes with $k_r^{\mathrm{B}} < 0$ correspond to an anti-parallel phase velocity and power flow along $\hat{\mathbf{x}}'$. The figure of merit (FOM) used for gauging the loss of the unit cell is the inverse of the loss tangent, $\left|k_r^{\mathrm{B}} / k_i^{\mathrm{B}}\right|$. Typical low-loss NIM unit cells at microwave frequencies [41] are characterized by a high FOM~100 and a narrow negative index band in the first Brillouin zone. This band has opposite phase and group velocities [78] (i.e. $k_r^{\mathrm{B}}(\partial\omega / \partial k_r^{\mathrm{B}}) < 0$), which is consistent with the Bloch mode in Fig. 2.4 with $k_r^{\mathrm{B}} \operatorname{sgn}(k_i^{\mathrm{B}}) < 0$, since the direction of the $x'$ component of group velocity, $\partial\omega / \partial k_r^{\mathrm{B}}$, is also along that of the power flow ($\operatorname{sgn}(k_i^{\mathrm{B}})$) in the limit of zero loss [79].

The hypotenuse of the prism is stepped, with prism angle $\theta = \arcsin(a / d) = \arcsin(1/\sqrt{1+l^2})$. Here, $d = \sqrt{1+l^2}\,a$ is the interface periodicity, and there are one and $l$ unit cells along $\hat{\mathbf{x}}'$ and $\hat{\mathbf{y}}'$ per step, respectively. The Bloch wave is impingent on the hypotenuse directed along $\hat{\mathbf{y}}$ at an apparent incidence angle, $\theta$, and excites reflected Bloch waves and transmitted plane waves. Obtaining transmission and reflection coefficients requires matching of these waves along the stepped hypotenuse with boundary conditions. Independent of details of a period on the interface, Bloch's Theorem dictates [72] the phase matching condition

$$\mathbf{k}_t^{\mathrm{B}} = \mathbf{k}_t^m + m\mathbf{G}, \tag{2.4}$$

where $\mathbf{G} = (2\pi / \mathrm{d})\hat{\mathbf{y}}$ , and $\mathbf{k}_t^m$ is the *complex* transverse wave vector of the $m^{\text{th}}$ transmitted diffraction order and reflected Bloch wave in the extended Brillouin zone scheme, as shown in Fig. 2.4. Since Bloch's Theorem does not require $\mathbf{k}_t^{\mathrm{B}}$ to be real [80], this equation applies even when $k_i^{\mathrm{B}} > 0$, i.e. in the presence of loss within the prism. In scalar form, this generalized phase matching condition can be written as:

$$\begin{cases} [k_r^{\mathrm{B}}]_y = [k_r^m]_y + m(2\pi / d) \\ [k_i^{\mathrm{B}}]_y = [k_i^m]_y \end{cases}, \tag{2.5}$$

where the subscript *y* denotes the scalar component along $\hat{\mathbf{y}}$. Both $k_r^{\mathrm{B}}$ and $k_i^{\mathrm{B}}$ are along $\hat{\mathbf{x}}$' also as a result of this phase matching condition. Since Bloch's Theorem derives from the discrete translational symmetry of the physical structure, Eq. 2.5 is independent of the possible nonzero power flow of the Bloch mode transverse to $\mathbf{k}^{\mathrm{B}}$ due to anisotropy [74]. Equation 2.5 is also independent of the types of waves involved and may apply to other periodic media.

In the far field, the propagating wave is a solution to the Helmholtz Equation with translational symmetry associated with phase factor, $\exp(ik_t^m y)$. This eigenmode in a lossless medium must be an inhomogeneous plane wave [81] with orthogonal planes of constant phase and amplitude. Its wave vector has both real and imaginary components along the normal to these two planes, as indicated by $\mathbf{k}_r^0$ and $\mathbf{k}_i^0$, respectively, in Fig. 2.4. The inhomogeneous plane wave amplitude diverges at $y \to \infty$, but in physical systems the wave is always bounded by a finite aperture. Declercq *et al.* [82] found that a single inhomogeneous plane wave component dominates the behavior of the bounded

wave. Indeed, the time-averaged power flow of a single inhomogeneous plane wave is predicted to be along the real wave (ray) vector $\mathbf{k}_r^0$ [81]. Such predictions, including those based on Eq. 2.5, have been experimentally verified at acoustical frequencies extensively [83-85].

The dispersion relation of an inhomogeneous plane wave is [81]

$$\left|\mathbf{k}_r^m\right|^2 - \left|\mathbf{k}_i^m\right|^2 = k_0^2, \tag{2.6}$$

where $k_0=2\pi/\lambda$ is the vacuum wave number. For $m$=0, solutions of $\mathrm{k}_r^0$ to Eqs. 2.5 and 2.6 are:

$$\left|k_r^0\right|^2 = \frac{1}{2}\{k_0^2 + (\left|k_r^{\mathrm{B}}\right|^2 + \left|k_i^{\mathrm{B}}\right|^2)\sin^2\theta \pm \sqrt{[k_0^2 + (\left|k_r^{\mathrm{B}}\right|^2 + \left|k_i^{\mathrm{B}}\right|^2)\sin^2\theta]^2 - 4\left|k_r^{\mathrm{B}}\right|^2 k_0^2 \sin^2\theta}\}. \tag{2.7}$$

In the lossless case, $k_i^{\mathrm{B}} = 0$, and Eq. 2.7 reduces to $k_r^0 = k_0$ or $k_r^0 = k_r^{\mathrm{B}}\sin\theta$. The former solution corresponds to a homogeneous plane wave ($k_i^0 = 0$) when $k_0 > k_r^{\mathrm{B}}\sin\theta$, while the latter corresponds to an evanescent wave propagating along the surface in the presence of total internal reflection when $k_0 \le k_r^{\mathrm{B}}\sin\theta$. When $k_i^{\mathrm{B}} > 0$, both $k_0^2$ and $(k_r^{\mathrm{B}}\sin\theta)^2$ are between the two solutions in Eq. 2.7, and the smaller (negative) solution is discarded, since Eq. 2.6 requires that $k_r^0 \ge k_0$. Higher order waves corresponding to $m\neq0$ can also be excited. Given that typically [38] $d\sim\lambda/2$ and, therefore, $G \sim 2k_0$, Eq. 2.6 shows $k_r^m \approx k_i^m$ □ $k_0$ for $m\neq0$. The imaginary component of Eq. 2.5 therefore implies that the corresponding rays will be at near-grazing angles and bound to the interface, as

indicated by $\mathbf{k}_r^{-1}$ and $\mathbf{k}_r^1$ in Fig. 2.4. This explains the existence of such beams in the numerical simulations in Fig. 2.3.

### 2. 3. 2 Comparison of Theory to NIM Refraction Experiments

Equation 2.5 implies that the real part of the effective index follows Snell's Law, viz:

$$n_r = \sin\theta_0 / \sin\theta = (k_r^{\mathrm{B}} / k_r^0)\,\mathrm{sgn}(k_i^{\mathrm{B}}), \tag{2.8}$$

where $\theta_0$ is the refraction angle for $m$=0. This index corresponds to the far-field power flow direction and is used for explaining experimental results. In the lossless case, Eq. 2.8 gives:

$$n_r = \begin{cases} (k_r^{\mathrm{B}} / k_0)\,\mathrm{sgn}(\partial\omega / \partial k_r^{\mathrm{B}}) \\ (1/\sin\theta)\,\mathrm{sgn}(\partial\omega / \partial k_r^{\mathrm{B}}) \end{cases} \text{when} \begin{matrix} (k_0 > k_r^{\mathrm{B}} \sin\theta) \\ (k_0 \le k_r^{\mathrm{B}} \sin\theta) \end{matrix}, \tag{2.9}$$

where the *sgn* function ensures that the group velocity is along $\hat{\mathbf{x}}'$, consistent with Eq. 2.2. Assuming parameters ($\theta$, $\lambda/a$, and FOM) typical of experimental unit cells [38, 41, 48, 61, 70], we calculate $n_r$ as a function of $k_r^{\mathrm{B}}$, with results shown in Fig. 2.5. FOM=3 typical of unit cells in the optical domain [48, 70] leads to a deviation of $n_r$ from Eq. 2.9 that is dependent on both $\theta$ and $k_r^{\mathrm{B}}$, particularly toward the edge of the Brillouin zone. These observations are qualitatively consistent with steady state full-wave simulations of $18^\circ$ and $26^\circ$ prisms (Fig. 2.3) consisting of the near-infrared frequency NIM in Sec 2.2. Quantitative experimental confirmations on the effect of imaginary transverse wave vector on the direction of diffracted inhomogeneous plane wave can be found in Refs. [83-85].

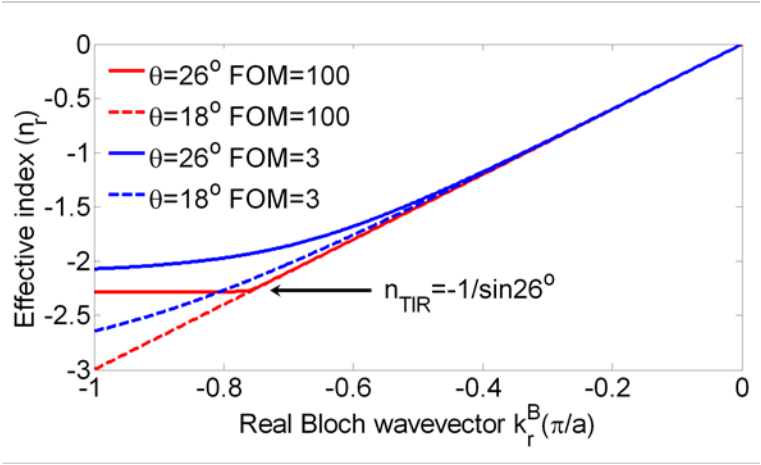


Fig. 2.5 Observed effective index $n_r$ calculated using Eqs. 2.7 and 2.8 in text. The parameters used in the calculation are: $\theta = 18^\circ$ (Refs. [38, 48, 61]), $26^\circ$ (Refs. [48, 61]); λ/a=6 (Refs. [38, 48, 61]); FOM=100 (Ref. [41]), 3 (Refs. [48, 70]). The frequency dispersion of the vacuum wave number, $k_0$, is neglected due to the narrow bandwidth of the negative index band. The lossless case (Eq. 2.8 in text) is nearly identical to that for FOM=100. Also, $n_{TIR}$ is the onset of total internal reflection in the lossless case for $\theta = 26^\circ$.

In contrast, the lossless case is nearly identical to the case for FOM=100, which is often observed at microwave frequencies [41]. This suggests that loss can be neglected for typical microwave NIM structures in refraction experiments. We calculated band structures of the unit cells in Refs. [41, 42] and derived the effective indices using Eq. 2.9. These two experiments used the same NIM structure to fabricate prisms with different angles ($\theta$), and the difference in working frequency is due to different absorption of the adhesives in unit cells used in two experiments [86, 87]. The agreement of the results with the experimental data is excellent, as shown in Fig. 2.6.

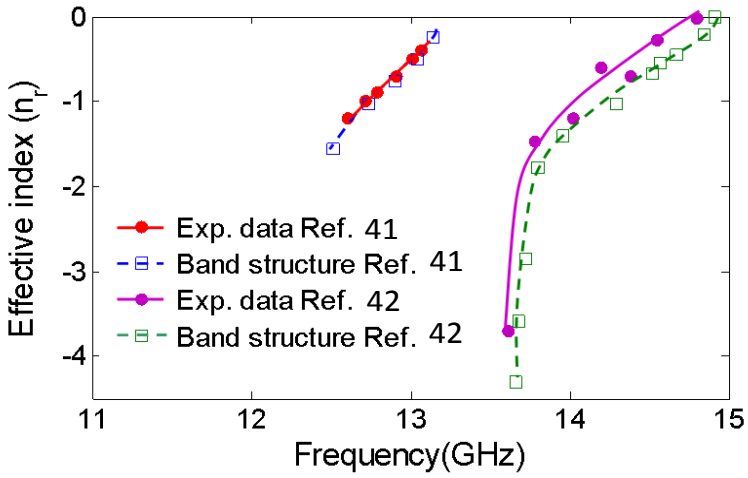


Fig. 2.6. Effective indices derived via Eq. 2.9 from calculated band structures of Refs. [41, 42]. Both are consistent with the experimentally measured values for these metamaterials. Solid and dashed lines are guide to the eye.

## 2. 4 Unified Explanation of Negative Refraction by NIMs and Photonic Crystals

In addition to NIMs, negative refraction has also been observed in lossless dielectric photonic crystals [44, 74]. These observations have been well understood as diffraction using the equi-frequency contour (EFC) approach, which is based on the same phase matching condition (Eqs. 2.1 and 2.4) as employed in Sec 2.3. Negative refraction typically occurs in dielectric photonic crystals at the ratio of unit cell size to wavelength of approximately 1/3 [44], compared to that of 1/6 for a metal-dielectric NIM [38]. Despite the lack of a clear distinction between the two types of periodic structures, negative refraction by NIMs has been suggested [88] to have a different origin than that observed in photonic crystals, which is due to Bragg diffraction.

NIMs refraction experiments [38, 41, 42] have been interpreted in EMT, assuming a homogeneous NIM, whose optical properties are due to a superposition of the negative $\varepsilon$

of metal wires [15] and the negative $\mu$ of the split ring resonators [25] that comprise the prism. The general treatment in Sec. 2.3 explicitly accounts for the inhomogeneity of the unit cell through a complex Bloch wave, but requires no assumptions about $\varepsilon$ and $\mu$. We have therefore provided a completely general explanation of negative refraction observed in both lossy NIMs and lossless photonic crystals. Indeed, band structures [78] calculated for the first reported NIM structure exhibiting negative refraction are also consistent with the experimentally measured indices [38] using $n_r = (k_r^{\mathrm{B}} / k_0)\,\mathrm{sgn}(\partial\omega / \partial k_r^{\mathrm{B}})$ , and are characterized by a dispersion relation $k_r^{\mathrm{B}}(\partial\omega / \partial k_r^{\mathrm{B}}) < 0$ within the first Brillouin zone. This "backward" Bloch band also accounts for negative refraction in lossless dielectric photonic crystals [44].

Although both EMT and the phase matching condition (Eq. 2.4) can describe NIM refraction experiments, their predictions may differ under certain circumstances. For example, Eq. 2.4 suggests that more than one far-field beam may be excited by the Bloch wave when the unit cell size is sufficiently large but still subwavelength, as is the case for some NIM unit cells. In past experiments [61, 68], such phenomena have been observed and explained as the diffraction by the stepped interface grating between air and a homogeneous NIM, which is equivalent to interpreting the Bloch wave vector $\mathbf{k}^{\mathrm{B}}$ in Eq. 2.4 to be that of a plane wave. If the stepped interface is linearized by using partial unit cells, EMT predicts the transmission of a plane wave through the planar interface between two homogeneous media, where the additional far-field beam disappears. However, the interpretation in terms of Bloch waves suggests that this beam is still present, since Eq. 2.4 derives from the translational symmetry of the periodic interface

only, independent of the details of a period. The observation of two propagating orders from a photonic crystal prism with a linear hypotenuse has been previously reported [89], where the angular positions of the far-field beams are consistent with Eq. 2.4. This difference is evidence for spatial dispersion, the deviation of the behavior of the NIM from its approximate local effective medium model.

The results presented here may also suggest the existence of a minimum unit cell size of optical NIMs. The maximum ratio of wavelength to periodicity currently achieved for optical NIMs is about 7, as will be discussed in Chapter 3. Tsukerman [90] has derived a minimum unit cell size imposed by a backward Bloch band for photonic crystals consisting of non-dispersive dielectrics. Since negative refraction by metamaterials is shown to be governed by the same Bloch band in the zero-loss limit, whether the minimum periodicity for NIMs containing dispersive metals at optical frequencies is restricted by a similar fundamental limit (apart from technological constraints) remains an open question.

## 2. 5 Summary

The general condition that must be met to observe negative refraction on a prism composed of subwavelength low-loss NIM unit cells is a dominant Bloch band that exhibits an oppositely directed wavevector and group velocity within the first Brillouin zone. The effective index is given by $n_{eff} = (k / k_0)\,\mathrm{sgn}(\partial\omega / \partial\,\mathrm{Re}(k))$. In addition, a near-infrared NIM design is presented with realistic material parameters. The geometrical parameters are compatible with a layer-by-layer approach for building a bulk

metamaterial [91]. Furthermore, based on a generalized phase matching condition, we have shown that the negative refractive behavior of lossless dielectric photonic crystals and lossy metal-dielectric periodic NIMs can be given a unified explanation. We have also discussed its implications for the effective medium model of NIMs as well as the possible existence of a minimum unit cell size for optical NIMs.

# CHAPTER 3

## Experimental Study of a Subwavelength Near-Infrared Negative Index Material

Optical negative index metamaterials (NIMs) [45, 46, 70] typically have a large unit cell size that is approximately half of the wavelength of operation in at least one dimension, unlike their microwave counterparts that are substantially subwavelength. This large periodicity makes the application of the effective medium theory (EMT) problematic [56, 92]. Moreover, while there have been a number of reports of optical NIMs [31], including a recent prism refraction experiment at a wavelength of $\lambda$=1.5μm [70], interferometric measurements of the phase advance of light at optical frequencies [93] have been rare. In the few reports of such experiments [46, 94], the relationship between the measured phase advance through samples consisting of only a single layer of unit cells and that expected from transmission through hypothetical multi-layer bulk NIMs was not investigated.

In this chapter, we describe the fabrication of a layer of the subwavelength near-infrared NIM structure introduced in Sec. 2.1, characterize its optical transmission, and measure the negative phase advance using a polarization interferometer. We also examine

the influence of losses and fabrication uncertainties on its potential bulk negative index properties using numerical simulations.

## 3. 1 NIM Fabrication and Transmission Spectra

The unit cell of the near-infrared NIM structure, subwavelength (~$\lambda$/7) in both the $\hat{x}$ and $\hat{y}$ directions and extending infinitely along the $\hat{z}$ direction, is shown in Fig. 3.1(a). The submicron features of the single layer NIM were patterned on a glass substrate with a Raith150 electron-beam writer. Several 100×100μm$^2$ patterns were written with varying Au strip widths ranging from 70 nm to 120 nm. Fiducial marks for alignment were defined in the first strip layer photoresist (poly-(methyl methacrylate) 495K, MicroChem, Corp.) step. To mitigate the charging effects due to the non-conductive substrate, a charge-dissipation polymer (Espacer 300Z, Showa Denko) was spun over the resist prior to exposure.

Following the deposition of the first layer of 20 nm thick Au at 5Å/s and lift-off of the photoresist in acetone, an approximately 40-nm thick layer of Benzocyclobutene (BCB, Cyclotene 3022-25, The Dow Chemical Company) diluted in mesitylene was spun onto the sample surface and cured in a nitrogen oven at 250$^o$C for one hour. The root mean square roughness of the polymer surface was measured with an atomic-force microscope to be <5nm, as shown in Fig. 3.1(b). The dielectric layer was then etched in a $CF_4$:$O_2$ plasma to attain a thickness of 10-20nm. Optical lithography was used to define 100×100μm$^2$ Ti(2nm)/Au(20nm) patches that covered the grating patterns, corresponding to the central metallic layer. Here the Ti layer enhances the adhesion of the Au to the

dielectric. Next, a second 40 nm thick dielectric layer was spun on and etched as above. The top strip layer consisting of 20 nm thick Au was similarly defined with electron-

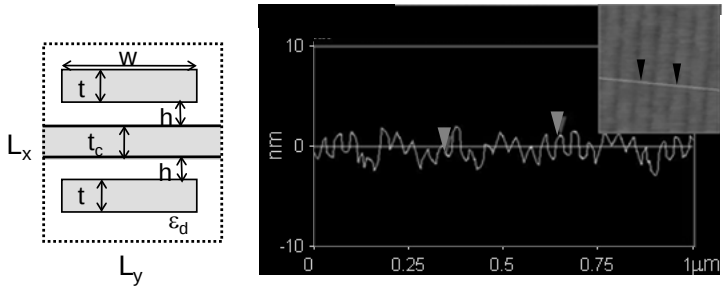


(a) (b)

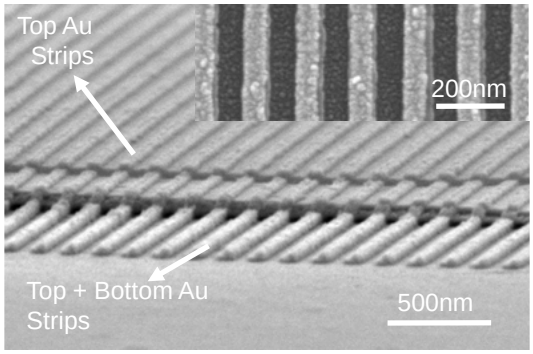


(c)

Fig. 3.1 (a) The unit cell. Lattice constants $L_x = L_y$= 150nm, Au strip and central layer thicknesses $t=t_c$=20nm, strip width $W$=100nm, and spacer thickness $h$=15nm. Gold strips and the central metallic layer are embedded in a polymer dielectric (cyclotene). (b) Atomic force microscope profile after planarization by the cured polymer on top of the Au grating pattern. The peak-to-valley roughness is 4.3 nm. *Inset*: The atomic force microscope image of the grating covered by the cured polymer, where the white line transverse to strips shows the cross section analyzed, and the marks correspond to their positions in (b). (c) Scanning electron microscope image of a completed structure. *Inset*: Top strips on top of the bottom strips at the edge of the pattern showing the alignment between them, where the central metallic layer is absent.

beam lithography as the bottom strip layer, followed by a second metal lift-off step. Scanning electron microscope (SEM) images of samples shown in the inset of Fig. 3.1(c) indicate that alignment to within 20 nm between top and bottom strip layers was achieved. The completed structure is shown in Fig. 3.1(c).

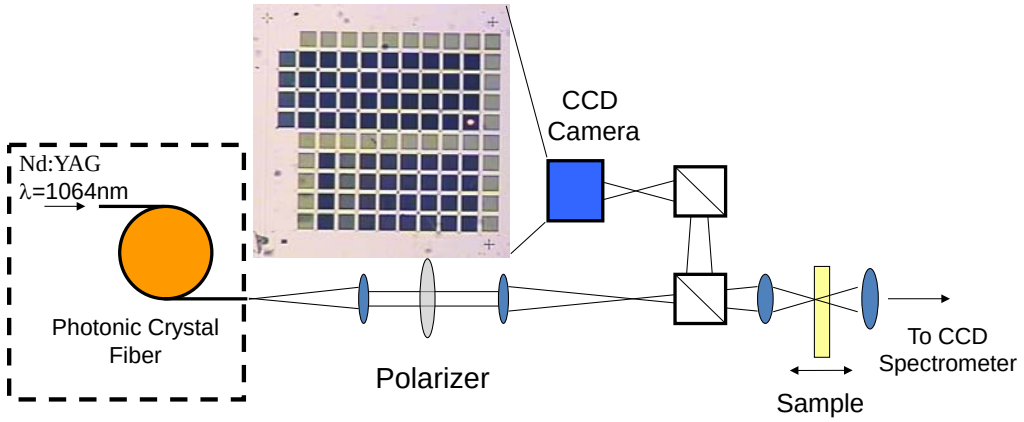


Fig. 3.2 Experimental setup for transmission spectra measurement. The array of the NIM sample blocks fabricated on a glass substrate is shown as the CCD camera image. The bright spot on the sample is the focused white light beam.

Fig. 3.2 shows the schematic of the transmittance spectra measurement setup, where the square patterns were illuminated with a ~20-$\mu$m-diameter, broadband supercontinuum laser beam obtained by coupling the output of a Nd-YAG pulsed laser into a photonic crystal fiber. The transmitted beam was analyzed with a spectrometer. Low-numerical aperture and visible/near-infrared achromatic objectives with long working distances were used for collimating and focusing the broad-band light. Spectra (relative to transmission through glass) for two patterns with an SEM-estimated strip width of 100nm are shown in Figs. 3.3(a)-(b). Also shown is the transmittance calculated using the Au

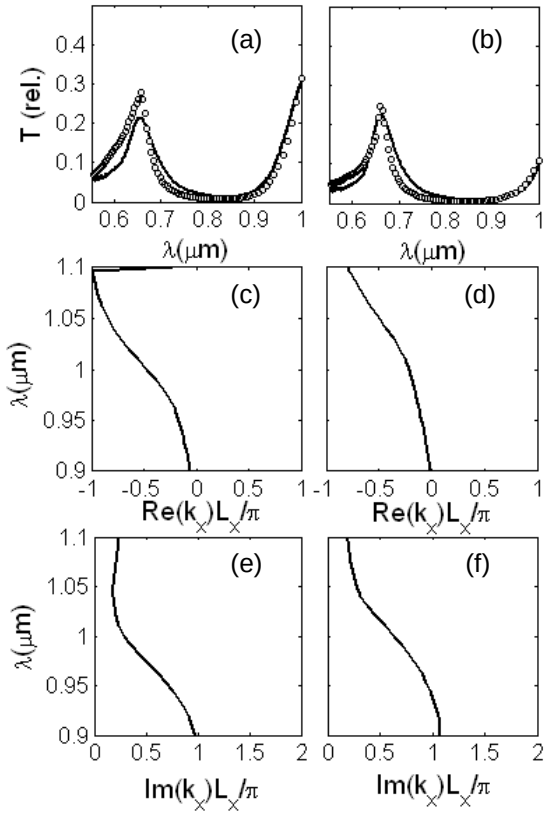


Fig. 3.3 (a)-(b) Transmission spectra for the NIM layers in Fig. 3.1. Continuous lines are experimental data; open circles are simulated results for structures with metal layer thicknesses $t=t_c$=22nm, top and bottom spacer thicknesses $h_{top}$=15nm and $h_{bot}$=9nm, respectively. Strip widths: (a) $W$ = 105nm; (b) $W$=110nm. (c)-(f) Calculated band structure of the dominant Bloch mode assuming the geometrical parameters of (a)-(b), respectively. Transmission spectra and band structure of the same geometrical parameters are in the same column.

dielectric constant [64], and the metal and dielectric layer thicknesses and strip widths measured for the samples studied. The refractive index for the dielectric layers was 1.56 from ellipsometry, and 1.45 for the glass substrate. The thicknesses of metal and dielectric layers and strip widths were adjusted within reasonable limits to yield quantitatively good fits to the measured transmission spectra in Figs. 3.3(a)-(b). That is, we used Au strip and central layer thicknesses of $t=t_c$=22nm, $h_{top}$=15nm and $h_{bot}$=9nm

for the top and bottom dielectric spacer layers, and strip widths $W$ =105 and 110nm, respectively. These dimensions are compiled in Table I along with calculated errors, which are defined as the ratio of the maximum absolute deviation to the nominal value.

Table I. Nominal and experimentally determined dimensions of the negative index material structure in Fig. 3.1. Relative fabrication errors of the various dimensions are shown.

| | Au layer thicknesses (nm) | Au strip widths(nm) | Top spacer thickness(nm) | Bottom spacer thickness (nm) |
|---|---|---|---|---|
| Nominal | 20 | 100 | 15 | |
| Pattern 1 | 22 | 105 | 15 | 9 |
| Pattern 2 | 22 | 110 | 15 | 9 |
| Relative error | 10% | 10% | 40% | |

We have shown in Sec. 2.2 that for an arbitrary low loss unit cell, the bulk effective refractive index, $n_{eff}$, that is consistent with Snell's Law is given by the result of photonic band calculations following: $n_{eff} = (k/k_0)\,\mathrm{sgn}(\partial\omega/\partial\,\mathrm{Re}(k))$, provided that a single Bloch band dominates, the losses are small, and the unit cell is small compared to the vacuum wavelength. Here, $k$ is the wavevector of the dominant band in the first Brillouin zone, $k_0$ is the free-space wave number, and $\omega$ is the angular frequency. The dispersion relation of the dominant Bloch band [65] for the unit cells corresponding to pattern 1 and 2 in Table I are shown in Figs. 3.3(c)-(f). In both cases, a low-loss negative index band at wavelengths $\lambda$>1$\mu$m, characterized by $k\cdot(\partial\omega/\partial\,\mathrm{Re}(k))<0$, is apparent. The slight red

shift of this band relative to the calculations in Sec. 2.2 is due to the fabrication errors. Accordingly, the existence of the low-loss band, together with the subwavelength feature size, provides a sufficient condition for negative refraction to occur.

## 3. 2 Interferometric Measurement of Negative Phase Advance

In this section, we present experimental evidence for negative phase advance through the NIM sample using a polarization interferometer. Numerical scattering simulations further suggest that the negative phase advance through the sample is consistent with that exhibited by a bulk, multi-layer material.

### 3. 2. 1 Experimental Setup

A schematic of the NIM sample with dimensions corresponding to pattern 1 in Table I is shown in Fig. 3.4. Note that the top and bottom capping dielectric layers in a complete NIM unit cell are not present in the NIM structure fabricated on a glass substrate.

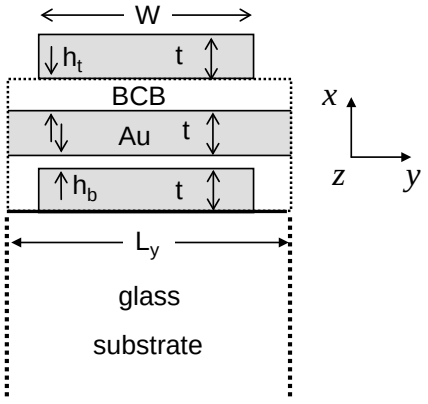


Fig. 3.4 Profile of the NIM sample fabricated on a glass substrate. Period $L_y$=$L$=150nm, Au strip and central layer thicknesses $t$=22nm, strip width $W$ =105nm, $h_t$=15nm and $h_b$=9nm for the top and bottom polymer dielectric (cyclotene) spacer layers.

Our approach to experimentally characterize the negative phase advance of the TM-polarized light is to interfere it with the TE-polarized light propagating through the same sample, and then to measure the relative phase advance ( $\Delta\varphi \equiv \varphi_{TM} - \varphi_{TE}$ ) using a polarization interferometer. The TE polarization is cut off inside the metamaterial, which serves as a wire grid polarizer. However, transmission of the TE polarization [95] is sufficient for our interferometry experiments. There are two features of this approach. First, both polarizations propagate through the same sample, so there is no need to account for their geometrical path difference. Second, it can be analytically shown (see below) that, because of the cutoff nature of the TE mode, $\varphi_{TE} < 0$. Therefore, $\varphi_{TM}$ is negative whenever $\Delta\varphi < 0$.

A polarization interferometer (Fig. 3.5) is used to measure the phase shift between orthogonally polarized states of light following a technique similar to that in [96]. We employ a tunable Ti:Sapphire ultrafast oscillator (~150-fs duration pulses at a repetition rate of 80 MHz) to perform measurements from $\lambda$=700 nm to 980 nm.

The laser beam is passed through polarizer P1, oriented at $45^{o}$ relative to the vertical. The polarization after P1 is the vector sum of horizontal and vertical components with identical phase. A microscope objective focuses this beam to a ~10$\mu$m diameter spot centered on the sample block. The sample is oriented such that vertically (TM) polarized light is expected to undergo a negative phase advance. Transmitted light is re-collimated by a second microscope objective. The two co-propagating polarization states then pass

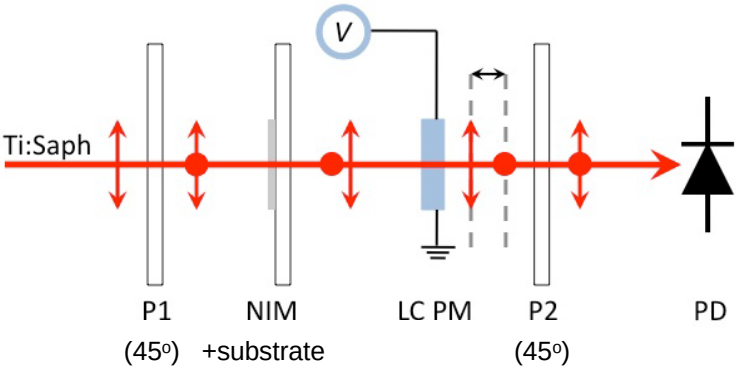


Fig. 3.5. Schematic of the polarization interferometer (top view). The light propagates from left to right. P1 and P2 are parallel oriented polarizers positioned 45° to the vertical, LC PM is a liquid crystal phase modulator, and PD is a photodiode. The two orthogonal polarization states (TE indicated by the arrows and TM indicated by dots) are in phase after polarizer P1, and experience different phase advances through the NIM sample and the liquid crystal phase modulator, as represented schematically by different positions of their phase fronts along the beam path.

through a liquid crystal variable phase retarder (LC) that introduces a controllable phase shift between the two polarizations. A compensator plate bonded to one window of the LC ensures this shift passes through zero at sufficiently high LC drive voltages. The light then passes through a second polarizer, P2, oriented parallel to P1, and is finally incident on a Si photodiode.

The photodiode voltage is proportional to the induced photocurrent and the incident optical power. Taking a time average over the period of optical oscillations, the measured photodiode voltage, $V_{pd}$, can be written as:

$$V_{pd} = \frac{E_{TM}{}^2 + E_{TE}{}^2}{2} + E_{TM} E_{TE} \cos(\varphi_{LC} + \varphi^0), \qquad (2.1)$$

since all voltage measurements have the same constant of proportionality relative to the electric field amplitudes. Here, positive constants $E_{TM}$ and $E_{TE}$ are the electric field amplitude of the two polarization states at the photodiode, $\varphi_{LC}$ is the relative phase shift

$\varphi$ introduced by the liquid crystal, and $\varphi^0$ results from other unintentional phase shifts between the two states, due either to residual birefringence in the sample or polarization rotation introduced by the optics.

The extrema voltages of the photodiode are given by:

$$V_{pd_{\max}}, V_{pd_{\min}} \propto \frac{{E_{TM}}^2 + {E_{TE}}^2}{2} \pm E_{TM} E_{TE}. \tag{2.2}$$

Using Eqs. 3.1-2,

$$\cos(\varphi_{LC} + \varphi^0) = \frac{1}{\Delta V}(V_{pd} - V_c), \tag{2.3}$$

where $V_c = (V_{pd_{\max}} + V_{pd_{\min}})/2$, $\Delta V = (V_{pd_{\max}} - V_{pd_{\min}})/2$, and $V_{pd}$ is a function of the variable phase advance between the two polarization states.

Figure 3.6(a) plots the photodiode voltage as a function of the LC drive voltage. These data are taken at a given wavelength for a reference sample consisting of an unstructured gold layer on the same substrate as the NIM. Using Eq. 3.3, we plot the wrapped phase ($\arccos(\varphi_{LC} + \varphi^0)$) as a function of LC drive voltage in Fig. 3.6(b). The periodicity of the cosine function introduces ambiguity in extracting the phase advance. However, the LC phase shift monotonically decreases with increasing drive voltage. Since $\varphi^0$ is within the domain ($-\pi, \pi$), this is sufficient to accurately determine the phase advance, obtaining the calibration result in Fig. 3.6(c). As the LC phase advance is wavelength dependent, it is necessary to obtain calibration data for every wavelength of interest.

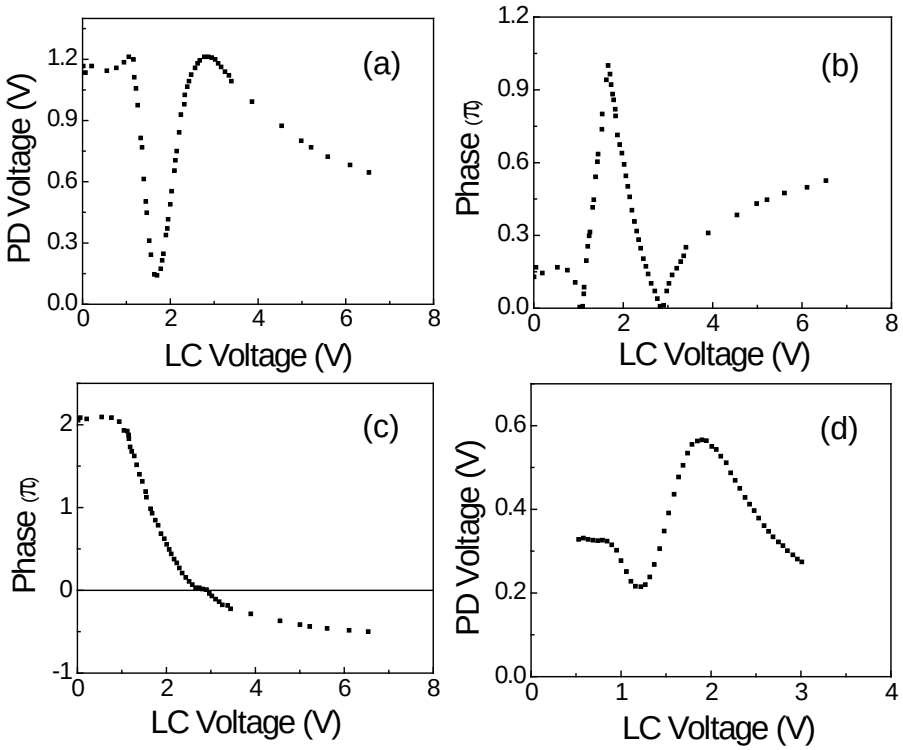


Fig. 3.6 (a) Photodiode voltage $V_{pd}$ as a function of the liquid crystal (LC) drive voltage at λ=886nm for an unstructured gold sample block used as a reference. (b) The wrapped phase as a function of LC drive voltage for the reference. (c) The unwrapped phase as a function of LC drive voltage for the reference. (d) $V_{pd}$ as a function of the LC drive voltage for a NIM sample block.

Equation 3.1 shows that the maximum photodiode voltage occurs when the phase shift due to the NIM is the additive inverse of the LC applied phase, which may be obtained from the calibration curve in Fig. 3.6(c). We thus obtain the relative phase shift due to the NIM by finding the LC drive voltage that produces the maximum of the photodiode voltage in Fig. 3.6(d). Note that the relative phase shift is determined only up to an additive constant of $m \times 2\pi$ ($m$ is an integer). As was shown in Sec. 2.2, the effective index of sufficiently thin samples determined for $m$=0 corresponds to the photonic band

structure of the unit cell within the first Brillouin zone, which is consistent with Snell's Law in a refraction experiment.

### 3. 2. 2 Phase Measurement Results

Numerically simulated $\varphi_{TM}$, $\varphi_{TE}$, and $\Delta\varphi$ between the two polarization states using the sample dimensions in Fig. 3.3 are plotted as continuous lines in Fig. 3.7(a), where the TM phase advance dominates the relative phase shift, as expected [63]. In these simulations, plane electromagnetic waves are assumed to be normally incident on, and scattered by the sample. The measured relative phase advances obtained for two sample blocks on the same substrate, are also plotted in Fig. 3.7(a) (open symbols). The random error in the photodiode voltage is <1%, as determined by repeated measurements. The uncertainty in LC drive voltage that corresponds to the maximum photodiode voltage is more significant due to the zero slope of the data at this point, resulting in an error of approximately 0.2rad in phase retrieval. Finally, the uncertainty in the actual sample dimensions may also be a significant source of error, as indicated by the differences between data taken on different sample blocks with identically designed structures.

To examine whether the negative TM phase advance exhibited by a single layer is consistent with the properties of a bulk medium with multiple layers of similar unit cells, the band structure $k_x$ was calculated [65] for TM polarized electromagnetic modes propagating in the $\hat{x}$-direction, assuming a periodic array of complete square unit cells (inset of Fig. 3.7(b)) capped with polymer dielectric layers with the same parameters as the fabricated sample in Fig. 3.4. When the number of layers is sufficiently large, the

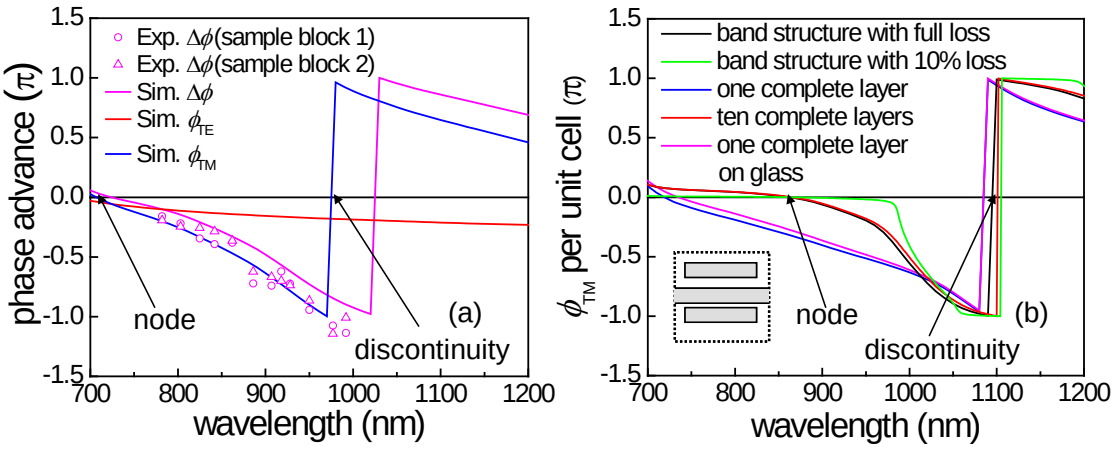


Fig. 3.7 (a) Measured relative phase shift $\Delta\varphi = \varphi_{TM} - \varphi_{TE}$ for two sample blocks fabricated on the same substrate with identically designed structure (open symbols). Calculated $\varphi_{TM}$, $\varphi_{TE}$, and $\Delta\varphi$, obtained from normal incidence plane wave scattering simulations assuming the sample in Fig. 3.4, are also plotted (lines). (b) Phase advance per unit cell for TM electromagnetic waves derived from the band structure using $\varphi_{TM} = \mathrm{Re}(k_x)L$, as well as those from scattering simulations. Here, $\varphi$ is the phase advance per unit cell, $k_x$ is the wave vector in the $\hat{x}$-direction. Inset: the complete unit cell with structural parameters in Fig. 3.4 and additional capping dielectric layers, whose periods $L_x$=$L_y$=$L$=150nm.

propagating electromagnetic wave is a Bloch mode, and the phase advance per unit cell, $\varphi_{TM} = \mathrm{Re}(k_x)L$, is a bulk property, as is shown in Fig. 3.7(b). The negative $\varphi_{TM}$ between λ=880nm and 1100nm, therefore, indicates a negative index band for light transmitted through a similarly structured periodic bulk medium. The negative index band of the bulk NIM (black line in Fig. 3.7(b)) resembles that simulated for a single layer (blue line in Fig. 3.7(a)). As will be further discussed in Sec. 3.3.2, this is due to the single cell resonance that is responsible for the negative index band and the weak inter-layer interaction, which is necessary for inferring the bulk optical properties from single layer measurements. There is, however, a substantial shift between the TM phase advances from scattering simulations in Fig. 3.7(a) and the calculated band structure in Fig. 3.7(b).

In particular, the node and discontinuity on the frequency axis that delimit the negative index band are shifted.

To understand the shift of the node, we exclude the influence of the substrate by numerically simulating the phase advance by a single layer of the complete unit cells, as shown in Fig. 3.7(b). It is significantly different from the phase advance derived from band structure due to surface effects of the single layer. Indeed, the simulated phase advance per unit cell by ten stacked, repeating layers is almost identical with that obtained from the band structure.

The discontinuity in the phase advance at $\lambda$=1100nm for both the single layer and ten stacked layers in Fig. 3.7(b) agrees with that of the band structure. The experimental sample in Fig. 3.4 is on top of glass substrate but without the capping polymer dielectric layers. To ascertain whether the shifted discontinuity at $\lambda$=970nm of the TM phase advance in Fig. 3.7(a) is due to the presence of the glass substrate or the absent capping polymer dielectric layers, we simulated the phase advance using a complete unit cell on a substrate. In this case, the discontinuity remains at around $\lambda$=1100nm. Hence, we infer that the frequency shift of the discontinuity in Fig. 3.7(a) is due to the missing capping dielectric layers in the fabricated sample.

Note that the phase advance for the tunneling TE mode is also negative. This phase advance occurs at the entrance and exit interfaces, and is a consequence [97] of the sub-barrier tunneling amplitude across a barrier of thickness $D$ which presents a purely imaginary refractive index $n = i\Gamma$ to the tunneling wave:

$$t = \frac{4i\Gamma}{(1+i\Gamma)^2 e^{\Gamma D k_0} - (1-i\Gamma)^2 e^{-\Gamma D k_0}}, \tag{2.4}$$

where $k_0$ is the vacuum wave number. In the weak-tunneling limit of $\Gamma >> 1$ and $\Gamma D k_0 >> 1$, the approximate expression for the tunneling amplitude is

$$t \approx 4/\Gamma \exp(-i\pi/2 + i2/\Gamma - \Gamma D k_0). \quad (2.5)$$

That the negative phase advance is a purely interfacial effect is clear from its independence of the layer's thickness.

## 3. 3 Losses and Fabrication Uncertainties

Using numerical simulations that include artificially low metallic losses, here we confirm that the negative effective index exhibited by this structure is not the result of high losses at optical frequencies [98]. Moreover, we show that the fabrication inaccuracies in the dielectric spacer thickness that are likely to be introduced in a prism composed of multiple layers of this structure are within a range that preserves its negative refractive behavior.

### 3. 3. 1 Role of Losses

It is understood that that the origin of the negative index of many optical NIMs is due to absorption, and their effective permittivity and permeability are not simultaneously negative [31]. For our NIM structure, even assuming a much reduced Au absorption from its actual value (e.g. 10% of the imaginary part of its actual permittivity), the calculated phase advance per unit cell (green line in Fig. 3.7(b)) still indicates a persistent negative index band, although it is narrower than that calculated taking into account the actual loss

of the Au strips (black line). In fact, the unit cell structure in Fig. 3.7(b) with two different spacings between the central continuous film and the metallic strips can be described as a bi-anisotropic medium, due to its lack of inversion symmetry [99]. Still assuming 10% of the imaginary part of Au permittivity and using the approach in Ref. [97] for extracting effective parameters from a reciprocal [99] bi-anisotropic medium, we calculated the effective index ($n_x$), permittivity ($\varepsilon_y$), permeability ($\mu_z$), and magnetoelectric coupling coefficient ($\xi_0$) for our structure. The results are shown in Fig. 3.8. The sign of Re($n_x$) is determined by requiring Im($n_x$)>0. In the (shaded) majority of the negative index band extending from $\lambda$=1000nm to 1070nm, the imaginary parts of all of the effective parameters are negligible compared with their real parts. Within this low-

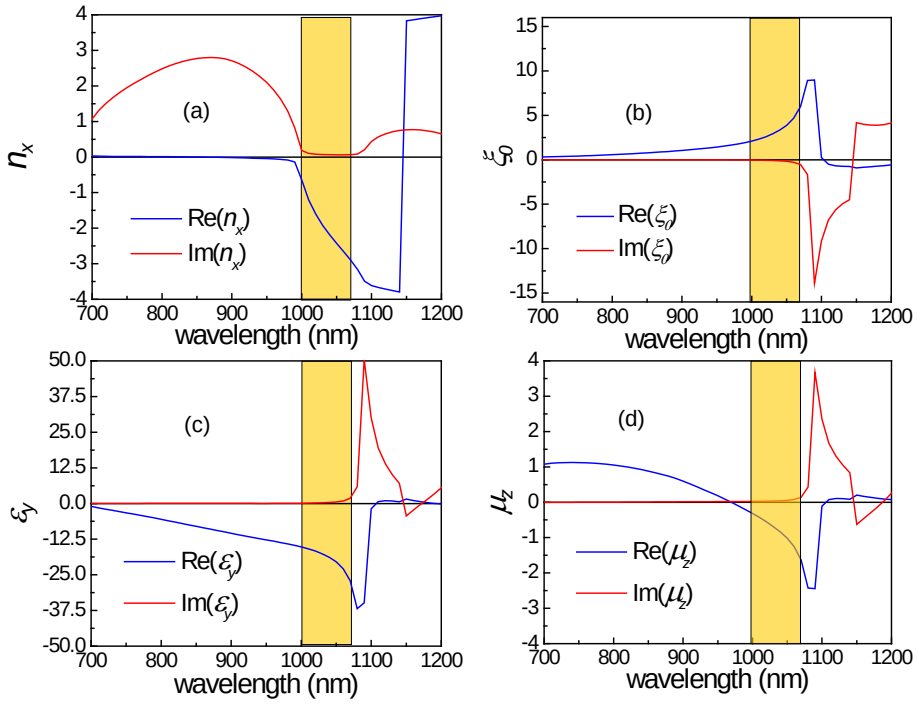


Fig. 3.8. Effective (a) index ($n_x$) (b) magnetoelectric coupling coefficient ($\xi_0$) (c) permittivity ($\varepsilon_y$) (d) permeability ($\mu_z$) calculated for our structure assuming 10% Au loss. The shaded region corresponds to the negative index band.

loss region, the dispersion relation of a propagating mode in a bi-anisotropic NIM [97], $n_x = -\sqrt{\varepsilon_y \mu_z - \xi_0^2}$ , requires simultaneously negative real parts of both the effective permittivity and permeability, regardless of the sign of Re($\xi_0$). Indeed, Re($\varepsilon_y$) and Re($\mu_z$) are both negative in this wavelength region. We caution, however, that these local homogeneous material parameters are approximate, and predictions based on their values may deviate from the macroscopic electromagnetic behavior of the composite, as we have discussed in Sec. 2.4.

### 3. 3. 2 Effect of Fabrication Uncertainties

We established in Sec. 3.1 the negative index for a potential bulk NIM through band calculations using the dimensions in Table I. Although we measured the negative phase advance through the single NIM layer consistent with this negative index (see Sec. 3.2), a bulk NIM fabricated with a layer-by-layer process [91] nevertheless inevitably has random fabrication uncertainties, which may shift or even eliminate the negative index band. It is, therefore, of interest to examine how the negative refractive behavior of the bulk will be affected by this randomness. Table I in Sec. 3.1 shows that of all the fabrication errors, the thicknesses of the dielectric spacer layers have the largest relative deviation due to their small dimensions and inaccuracies in the plasma etching process. We have, therefore, simulated a 3D prism composed of the unit cells of Fig. 3.1(a), where the angle of the hypotenuse is $18^o$. The dielectric spacer thickness (and hence the vertical position of each metal strip layer) is subject to a fabrication error that is simulated by a random variable in the range of [-7.5, 7.5] nm. Other sources of fabrication errors are

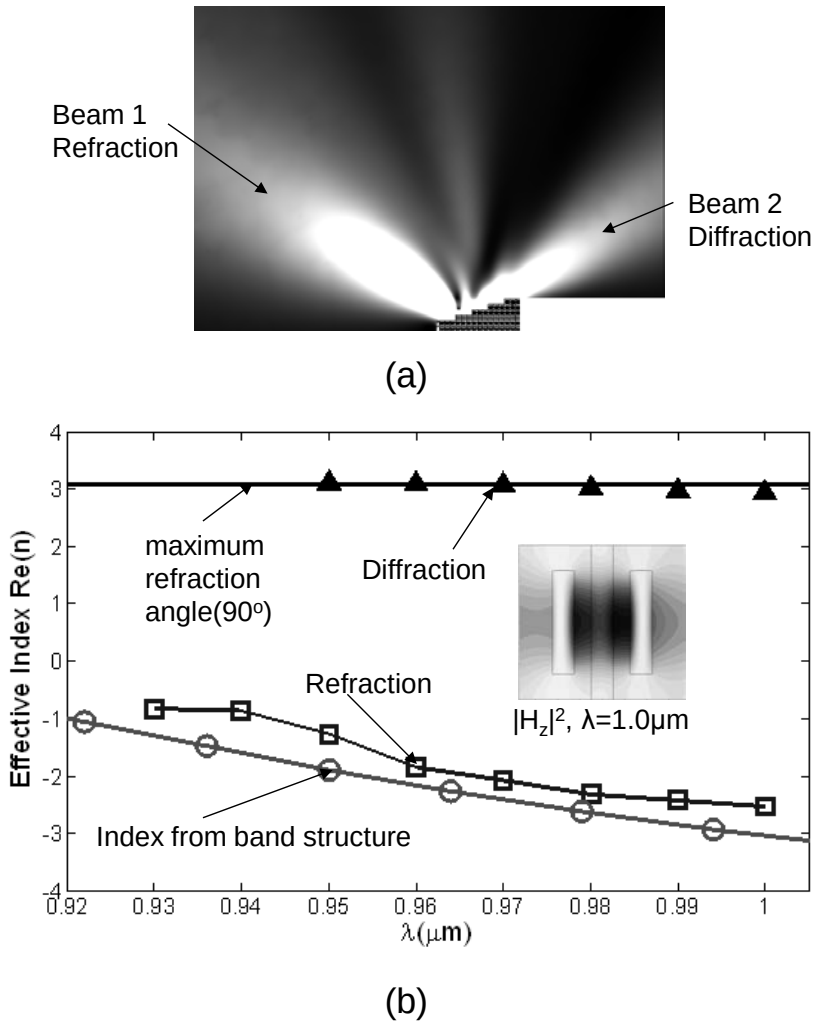


Fig. 3.9 (a) Time averaged power flow for a prism at an incident wavelength of λ=970nm. The dark background corresponds to nearly zero power flow. Disorder is introduced into the metal strip positions in the prism. Two far-field beams (1 and 2) are observed. (b) Comparison of effective indices extracted from numerical simulations and band structure calculations. Circles: Index calculated from the band structure of unit cell in Fig. 3.1(a). Squares: negative refraction. Triangles: diffraction. The horizontal line represents the angular position parallel to the hypotenuse. *Inset:* Amplitude of the magnetic field, $H_z$, of the Bloch mode of the unit cell in Fig. 3.1(a) at a wavelength of λ=1μm. Darker shade represents a larger field.

neglected since they are considerably smaller in relative magnitude. In the simulation, the $TEM_{00}$ mode of a parallel metal plate waveguide is normally incident upon the bottom of the prism.

A representative field plot at $\lambda$=970nm is shown in Fig. 3.9(a). In most situations, there are two far-field beams. The angular positions of the transmitted beams are used to determine the refractive indices, which are plotted in Fig. 3.9(b), together with the index of refraction calculated from the band structure of the unit cell of Fig. 3.1(a). The different frequency dependences of the two beams reveal their respective physical origins: Beam 1 (Fig. 3.9(a)) corresponds to the refracted beam, with its angular position consistent with predictions from Snell's Law. This indicates that the negative refractive behavior is relatively insensitive to fabrication errors in the strip position and spacing. This insensitivity can be understood by inspection of the field profile of the plasmonic resonance, with its magnetic field concentrated between the two metal strips, as shown in the inset of Fig. 3.9(b). This resonance is responsible for the increased transmission in the negative index band. The resonances in neighboring unit cells are weakly coupled, and therefore insensitive to the disorder. Beam 2 is a diffraction order that lies nearly parallel to the hypotenuse due to loss, as has been explained in Sec. 2.3.

## 3. 4 Summary

A single layer of a subwavelength near-infrared NIM structure was fabricated, which has a ratio of wavelength to periodicity of approximately 7. To our knowledge, this ratio is the highest among all experimental NIMs working at optical frequencies. The phase

advance by this NIM sample has been measured, and is consistent with numerical simulations of the bulk properties of an infinite medium composed of the NIM unit cells. Apart from fabrication and experimental uncertainties, the disagreement between experiment and the predictions of phase advance from the band structure model is likely due to surface effects introduced by employing only a single-layer unit cell sample lacking capping dielectric layers. Its fabrication errors and uncertainties are shown through numerical simulations to be within a range that preserves the negative index properties of the layers if employed in a bulk NIM.

# CHAPTER 4

## Microscopic Theory of Perfect Lensing

In 2000, Pendry postulated [27] that it may be possible to synthesize composite media with a negative refractive index. Modeling these composites as effective media and using negative permittivity ($\varepsilon$) and permeability ($\mu$) in macroscopic Maxwell equations, he predicted negative refraction, consistent with Veselago's earlier results [6]. Pendry further used the effective medium theory (EMT) to calculate transmission ($T$) of plane waves through an imaging system consisting of a flat slab made of these composites. The predicted limit of $T$ when both $\varepsilon$ and $\mu$ approach -1 is unity, independent of the transverse wave-vector of the incident radiation. This suggests that such a slab would result in a perfect (i.e., diffraction-free) image of a point light source, since it would restore all Fourier components of the optical field of an object, including evanescent waves. Ref. [27], therefore, lays out a road map for constructing a superior optical imaging device using negative refraction. The flat lens made of $\varepsilon=\mu=-1$ materials (the Veselago-Pendry lens) is therefore named the "perfect lens" or "superlens".

Negative refraction governed by Snell's law with a negative index ($n$) was subsequently observed [38, 41, 42] in metal-dielectric periodic composites with a subwavelength unit cell size, which are now known as negative index metamaterials (NIMs). Interpretations of these experiments invoke a homogenization procedure that computes the effective permittivity ($\varepsilon_{eff}$) and permeability ($\mu_{eff}$) of the NIM by approximating it as a local, homogeneous material. The obtained negative $\varepsilon_{eff}$ and $\mu_{eff}$ are further explained as the consequences of electric and magnetic resonances, respectively, and used in EMT to interpret the observed negative refraction, where $n = -\sqrt{\varepsilon_{eff}\,\mu_{eff}}$ .

Veselago-Pendry lenses require an object-image distance twice the thickness of the $\varepsilon$=$\mu$=-1 NIM slab. Recent experiments on such structures have been performed at microwave frequencies using NIMs comprised of transmission line (TL) networks [100, 101]. Experiments that do not satisfy these conditions have also been performed on other periodic material systems [102, 103]. For example, a NIM sample [102] consisting of 3 layers of unit cells provides the best resolution at 3.74 GHz among all such experiments, but its index of $n$=-1.8 in EMT would not allow focusing [104]. The resolutions demonstrated by these experiments (whether or not satisfying the above conditions), however, do not match those of available sub-diffraction-limit optical imaging techniques, such as scattering near-field scanning optical microscopes [105], with resolutions of 10nm at visible or longer wavelengths.

## 4. 1 Prior EMT Models on Perfect Lensing

Absorption has been found to prevent NIMs from acting as perfect lenses [106-110]. Therefore, superconducting elements have been proposed [108] to reduce absorption in

the lossy metal components of NIMs. More recently, experiments on all-dielectric [111] and gain-assisted [112] NIMs have demonstrated the possibility of reducing or eliminating absorption. In the latter case, the dominant limiting factor may be the inherent microstructure of composites.

Previous models [106-110, 113] that discuss the performance of perfect lensing have not quantitatively investigated the effect of NIM microstructure, since its existence is incompatible with EMT as employed in these studies. Alternative approaches include the use of an equivalent circuit model based on electromagnetic fields on the periodic lattice in TL NIM networks [114]. Some of these works [108, 113, 114] recognize that the resolution is limited by periodicity of the NIM slab.

Microscopic theories provide an alternative to modeling composites. Rather than assuming a single constitutive relation for the entire composite using $\varepsilon_{eff}$ and $\mu_{eff}$ obtained from a homogenization approximation, these models use the respective $\varepsilon$ and $\mu$ for each constituent, thereby preserving the physics of the microstructure. Examples of such theories are scattering and eigen-mode calculations based on the "microscopic" Maxwell's Equations. In contrast, the macroscopic approach of EMT neglects the effect of internal structure of a composite. Typical unit cell sizes ($d_c$) of NIMs [38, 41, 42] are between 1/10 and 1/6 of the wavelength ($\lambda$). Currently, the smallest $d_c/\lambda$ achieved at optical frequencies is approximately 1/7, which was discussed in Chapter 3. Given the practical and possibly fundamental constraints [90] on reducing the NIM unit cell size to yet smaller scales, EMT with $\varepsilon_{eff}$ and $\mu_{eff}$ may not adequately approximate the unusual effects associated with metamaterials [115, 116]. For example, the recent comparison

[117] of a microscopic model and EMT on chiral metamaterials has shown that the microstructure effects nearly reverse the repulsive Casimir forces predicted from EMT [118]. It is therefore of interest to compare $T$ in a microscopic model with the result in Ref. [27].

Here, we design a model $\varepsilon_{eff} = \mu_{eff} = -1$ NIM based on Mie resonances in cylinders with positive permittivity and permeability. The transmission through such a NIM slab is determined using both EMT and a microscopic model, and is used to predict the image profile of a point source. We then compare both results with full wave simulations of "imaging" of a point light source by the NIM lens, and find that EMT significantly overestimates the range of evanescent waves that can be recovered. We finally discuss the implications of our results.

## 4. 2 NIM Design and Homogenization

The model metamaterial structure is based on localized Mie resonances in circular rods [111, 119, 120]. Here we adopt the photonics crystal convention, where vacuum permittivity, permeability, and light velocity are dimensionless and equal to unity, and electromagnetic properties of the composite constituents are assumed to be frequency independent. This separates the effect of the unit cell microstructure from dispersion of the constituent materials at the frequency of interest.

The cross section of the hexagonal unit cell of the NIM in the $x$-$y$ plane is shown in Fig. 4.1, consisting of a cylinder embedded in air. The structure is infinitely long in the $z$

direction (perpendicular to the plane of the diagram). The total cross sectional area of the unit cell is 1 (hexagon side length $d$=0.6204), and the core radius, $r_s$=0.081. The core permittivity ($\varepsilon_s$=600) has been used in simulations of a NIM made of $Ba_{0.5}Sr_{0.5}TiO_3$ [111]. Its permeability ($\mu_s$=12) is an isotropic approximation to single-crystal yttrium-iron garnet that is used in Ref. [121] for NIM simulations. Since the Wigner-Seitz cell that defines the first Brillouin zone is also a hexagon, two different directions in the reciprocal space, Γ-X and Γ-M, are also shown in Fig. 4.1.

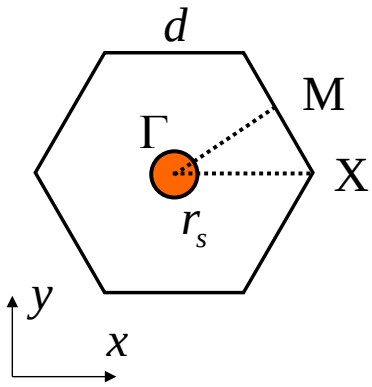


Fig. 4.1 The hexagonal NIM unit cell with side length, $d$=0.6204, and core radius, $r_s$=0.081. Two different directions (Γ-X and Γ-M) in reciprocal space are also shown.

We consider transverse electric (TE, $\mathbf{E} = E\hat{z}$ ) polarized electromagnetic waves propagating in the $x$-$y$ plane. The rods support Mie resonant modes of different orders, the first two of which correspond to the electric and magnetic responses of the composite [111, 119], respectively. Due to the inversion and six-fold rotational symmetries of the NIM unit cell, its constitutive relations in the local effective medium model are free of magneto-dielectric coupling [122], the relevant permittivity tensor component is $\varepsilon_{zz}=\varepsilon_{eff}$, and the permeability tensor must be diagonal and uniaxial [3] with $\mu_{xx}=\mu_{yy}=\mu_{eff}$. We

determine $\varepsilon_{eff}$ and $\mu_{eff}$ as functions of frequency ($f$=1/$\lambda$) using a homogenization theory which is based on the principle that a composite embedded in a homogeneous medium with its own $\varepsilon_{eff}$ and $\mu_{eff}$ should be free of scattering, and is therefore the electromagnetic analogue to the coherent potential approximation (CPA) in condensed matter physics [123]. This theory was first used by Lewin [124] to homogenize dielectric spheres, and has since been generalized and applied in a number of works [125-128], including the treatment of acoustic metamaterials with both negative bulk modulus and mass density [129]. For our 2D NIM, $\varepsilon_{eff}$ and $\mu_{eff}$ are obtained [130] using:

$$\frac{\varepsilon_{eff}+\dfrac{2J'_0(k_0r_0)}{k_0r_0J_0(k_0r_0)}}{\varepsilon_{eff}+\dfrac{2Y'_0(k_0r_0)}{k_0r_0Y_0(k_0r_0)}}=\frac{Y_0(k_0r_0)}{iJ_0(k_0r_0)}\left(\frac{D_0}{1+D_0}\right) \quad , \tag{4.1}$$

$$\frac{\mu_{eff}-\dfrac{J_1(k_0r_0)}{k_0r_0J'_1(k_0r_0)}}{\mu_{eff}-\dfrac{Y_1(k_0r_0)}{k_0r_0Y'_1(k_0r_0)}}=\frac{Y'_1(k_0r_0)}{iJ'_1(k_0r_0)}\left(\frac{D_1}{1+D_1}\right) . \tag{4.2}$$

Here, $k_0$=2$\pi f$ is the free space wave number, $r_0$=$\pi^{-1/2}$, $J$ is the Bessel function of the first kind, $Y$ is the Neumann function, and $D_0$ and $D_1$ are Mie scattering coefficients of the first two orders given by:

$$D_m=\frac{k_sJ'_m(k_sr_s)J_m(k_0r_s)-\mu_sk_0J_m(k_sr_s)J'_m(k_0r_s)}{\mu_sk_0J_m(k_sr_s)H'^{(1)}_m(k_0r_s)-k_sJ'_m(k_sr_s)H^{(1)}_m(k_0r_s)} , \ m=0, 1. \tag{4.3}$$

Here $k_s$= $k_0$ $(\varepsilon_s\mu_s)^{1/2}$ is the wave number in the core of the unit cell, and $H^{(1)}$ is the Hankel function of the first kind. For real $\varepsilon_s$ and $\mu_s$, both $\varepsilon_{eff}$ and $\mu_{eff}$ are correspondingly real

[130]. Furthermore, $\varepsilon_{eff}$ and $\mu_{eff}$ correspond to the electric and magnetic dipole densities in the long wavelength limit [119], respectively.

Both $\varepsilon_{eff}$ and $\mu_{eff}$ have been calculated for $0<f<0.12$, and are plotted in Fig. 4.2(a), where one magnetic and two electric resonances are apparent. In EMT, the frequency region with $\varepsilon_{eff}$ and $\mu_{eff}$ of the same sign corresponds to a real refractive index, or a pass band. The dispersion relation is therefore predicted using $k = 2\pi f\sqrt{\varepsilon_{eff}\mu_{eff}}$, where $k$ is the wave vector. The dispersion is plotted in Fig. 4.2(b) together with the band structure

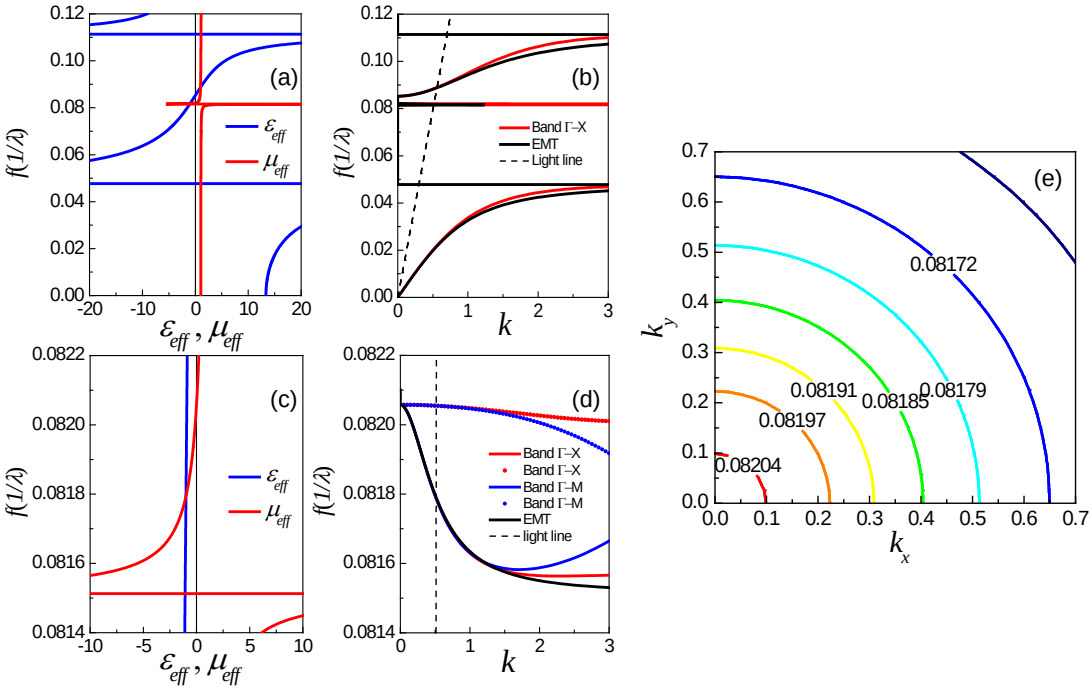


Fig. 4.2 (a). $\varepsilon_{eff}$ and $\mu_{eff}$ of the model NIM calculated from the homogenization theory. (b) The dispersion relation predicted from effective medium theory (EMT) and the numerically calculated band structure. (c-d) Details of the narrow negative index band with the calculated band structure in both the Γ-X and Γ-M directions. (e). Circular equi-frequency contours of the negative index band showing the isotropic nature of the model NIM.

numerically calculated using a finite-element solver (COMSOL, Inc.). Details of the narrow negative index band at approximately $f$=0.082 are shown in Figs. 4.2(c)-4.2(d), with numerically calculated band structure in both the Γ-X and Γ-M reciprocal lattice directions. In both Figs. 4.2(b) and 4.2(d), the agreement of the results from the two types of calculations is excellent, except at large $k$ that is far from the center of the first Brillouin zone. In Fig. 4.2(d), the nearly flat band (dots) immediately above this negative index band is due to symmetry degeneracy not captured by the homogenization theory [119], and has no effect on the electromagnetic properties of the NIM at the frequency of interest in Sec. 4.3. The numerically calculated equi-frequency contour of the negative index band (Fig. 4.2(e)) further exhibits the isotropic dispersion relation in the $k_x$-$k_y$ plane for our model NIM.

## 4. 3 Transmission and Image Profile

At the wavelength of interest, $\lambda$=12.226, corresponding to $f$=0.08179, which is near the crossing point of the NIM dispersion relation and the light line in Fig. 4.2(d), then $\varepsilon_{eff}$=-0.9880, and $\mu_{eff}$=-0.9983, or very close to the desired $\varepsilon_{eff}$=$\mu_{eff}$=-1. The ratio of wavelength-to-unit cell size is approximately 12, which is comparable to the experimentally demonstrated all-dielectric NIM [111], and twice that of a typical metal dielectric NIM [38]. Note that ($\varepsilon_{eff}$, $\mu_{eff}$) may be adjusted arbitrarily close to (-1, -1) by varying $r_s$ and $f$, but at a certain point the transmission through the NIM lens in both models will remain unchanged for transverse wave-vectors within the first surface Brillouin zone (SBZ). We focus our attention to the first SBZ, since previous work [114,

131] has indicated that the restoration of evanescent waves by the NIM slab will not be present beyond its boundary.

We consider a plane wave, $\exp(i(k_x x + k_y y))$, incident on an infinitely wide 5-layer NIM lens as shown in Fig. 4.3(a), where $k_x$ and $k_y$ are $x$- and $y$-components of the wave vector, $\vec{k}$. The ratio of the slab thickness-to-wavelength is comparable to experiments [100, 101]. The surface ($a$) and longitudinal ($b$) periods, are 1.0746 and 1.8612, respectively. The boundary of the first SBZ is therefore at $k_x = \pi / a = 5.69 k_0$.

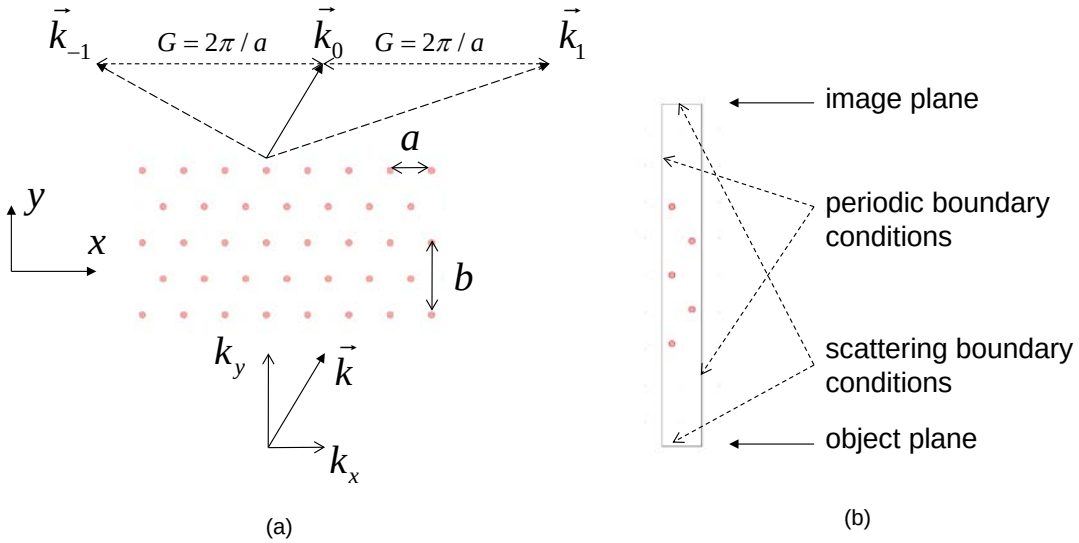


Fig. 4.3 (a). A plane wave incident on an infinitely wide 5-layer NIM lens with lattice constants $a$ =1.0746, and $b$=1.8612. Here, $k_x$ and $k_y$ are $x$- and $y$-components of the wave vector, $\vec{k}$. $\vec{k}_m$ is the wave vector the m$^{th}$ transmitted order, and $\vec{G} = (2\pi / a)\hat{x}$ is reciprocal surface unit mesh vector. Note that wave vectors of higher orders here are only illustrative, which in fact have substantial imaginary $y$-components (not shown) that correspond to their rapid decay in the $y$-direction. (b). The geometry used to calculate the transmission coefficient using a single period of the lens. The object-to-image distance is twice lens thickness.

In EMT, the transmission coefficient ($T$) of the incident wave is calculated using the result of Ref. [27] for $\varepsilon_{eff}$ and $\mu_{eff}$. In the microscopic model, the entire material system has discrete translational symmetry along the $x$-axis, and the wave vectors of the transmitted plane waves are therefore related by $\vec{k}_m = \vec{k} + m\vec{G}$, where $m$ is an integer that denotes the order of diffraction, and $\vec{G} = (2\pi / a)\hat{x}$ is the surface mesh reciprocal lattice vector. Since the NIM unit cell is significantly smaller than $\lambda$, coupling to higher orders that decay more rapidly in the $y$-direction in this case is weak [131]. We therefore consider the transmitted wave entirely due to the $0^{th}$ order (plane wave), which will be further confirmed by its consistency with full-wave simulations. We then make use of the $x$-periodicity to calculate the transmission coefficient with only a single period in COMSOL using scattering simulations. The geometry is shown in Fig. 4.3(b), where periodic boundary conditions enforce the lateral phase shift per period, $\exp(ik_x a)$. The image and object planes are symmetrically separated at twice the slab thickness, and are

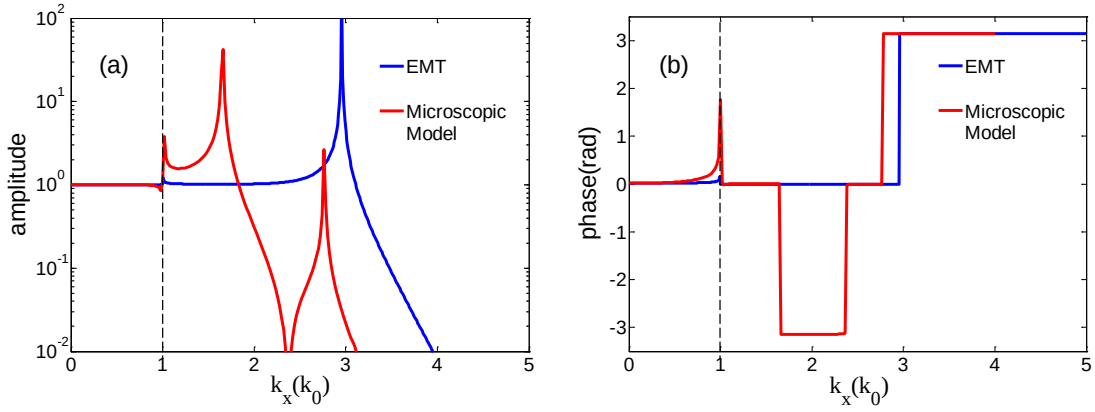


Fig. 4.4 (a) Amplitude and (b) phase of the transmission coefficient calculated for a 5-layer NIM lens using both the microscopic and macroscopic approaches.

governed by scattering boundary conditions that permit passage of plane waves without scattering. We perform the calculations using the scattered-field formulation in COMSOL, which allows for the separation of the incident and scattered fields. The transmission, $T$, is therefore given by the ratio of the total field at the image plane to the incident field at the object plane. Results of the amplitude and phase of $T$ from both EMT and the microscopic model are plotted in Figs. 4.4(a) and (b), where the dashed lines separate propagating ($k_x<k_0$) from evanescent waves ($k_x>k_0$).

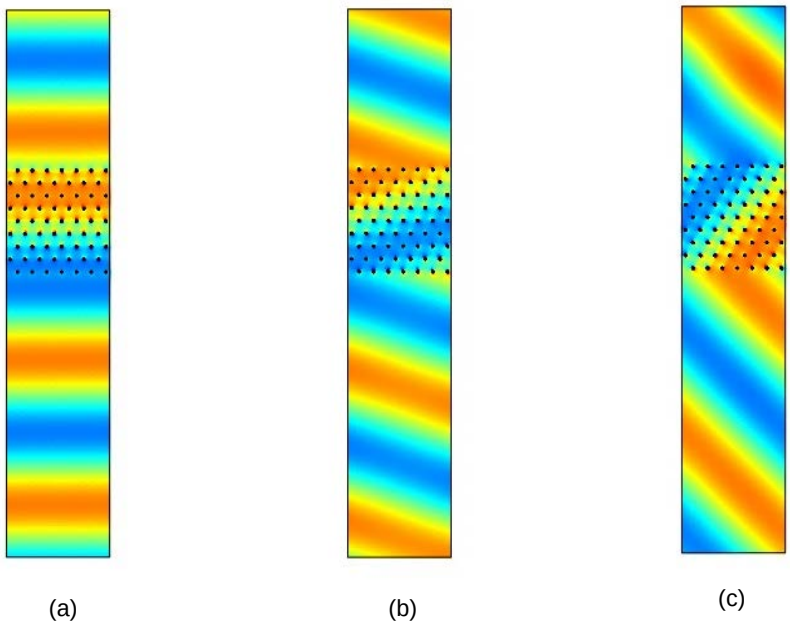


Fig. 4.5 Numerical scattering simulations of propagating waves through a 9-layer NIM slab at (a). $\sin\theta=0$. (a). $\sin\theta=0.3$. (c). $\sin\theta=0.707$. Here, $\theta$ is the incidence angle to the NIM slab surface. A 5-layer NIM slab has the same behavior.

For propagating waves ($k_x<k_0$), the two models are remarkably consistent, except near $k_x=k_0$, implying that the NIM is likely to exhibit nearly zero reflection and complete transmission of propagating waves, as predicted by EMT. This is confirmed by full-wave scattering simulations at different incident angles, as shown in Figs. 4.5(a)-4.5(c). The slabs are 9 layers thick to clearly show the phase evolution in the NIM, although 5 layer thick slabs have the same behavior.

In contrast, strong deviations between EMT and the microscopic model are found throughout the range of $k_x$ for evanescent waves ($k_x>k_0$). The apparent transmission peak for EMT in Fig. 4.4(a) is due to resonant excitation of the slab plasmon polaritons of the flat lens [108]. These modes result from coupling between the surface plasmon polaritons at the two interfaces of the NIM slab [132]. Similar resonant excitation by a point source has also been studied in the context of conventional optical waveguides and are associated with Purcell effect [133]. Figures 4.4(a) and 4.4(b) show that in EMT, the NIM lens is capable of transmitting evanescent waves up to $k_x$ of approximately $3k_0$ without a change in amplitude or phase. This should result in a subwavelength image of a point light source, and the deviation of $T$ from unity for other Fourier components corresponds to aberrations.

In the microscopic model, the peaks in the evanescent wave transmission spectrum also correspond to resonant excitation of slab plasmon polaritons, which have been studied in detail and referred to as “bound slab photon modes” in Ref. [131]. Figure 4.4(a) shows that the NIM microstructure significantly modifies the dispersion relation of the plasmon polaritons. Multiple layers of the unit cell lead to an increase in the number

of polariton modes and therefore transmission resonances [131]. Moreover, the wave numbers that correspond to transmission resonances and the node on $k_x$ axis are shifted significantly toward zero, which implies that the range of recoverable evanescent waves is reduced. We therefore expect that EMT will underestimate the width of the central peak of the image, which can be interpreted as the resolution limit of the NIM lens. For those recoverable evanescent waves, a range of $k_x$ with unity transmission is absent in the microscopic model. The complicated structure in transmission and phase as shown in Figs. 4.4(a) and 4.4(b) is expected to result in a greater degree of image aberration compared to EMT prediction [134].

In both models, small transmission resonances are visible at $k_0$ [108, 131, 134], which may be due to the opening of the evanescent wave channel for transmission to the image plane that is within the near field of the NIM lens. This type of effect is commonly known as a "threshold anomaly" [135]. Note also that all phase changes of $\pi$ in Fig. 4.4(b) that accompany the resonant transmission of evanescent waves (Fig. 4.4(a)) are abrupt steps, since the system is free of loss in both models. This observation is consistent with previous work [134].

We have numerically simulated imaging by a 5-layer thick NIM slab that is 47 surface periods wide (Fig. 4.6), in a geometry surrounded by absorbing perfectly matched layers (PMLs) that simulate infinite free space. The point electrical current source, $\vec{I} = \delta(x)\delta(y)\hat{z}$, emits TE-polarized field, where the time harmonic phase factor has been dropped. The profile of the emitted field is a Hankel function of the second kind, which approximates a $\delta$-function. The normalized field profile, $|E|^2$, in the image plane is shown in Fig. 4.7(a).

The predictions of the image profile from $T$ in both EMT and the microscopic model using the inverse Fourier transform:

$$E = \int_{-\infty}^{\infty} \exp(ik_x x) T(k_x) dk_x \tag{4.4}$$

are also plotted. Both integrals are evaluated using a finite difference summation between $k_x$=-5$k_0$ and $k_x$=5$k_0$ with $\Delta k_x = k_0/100$.

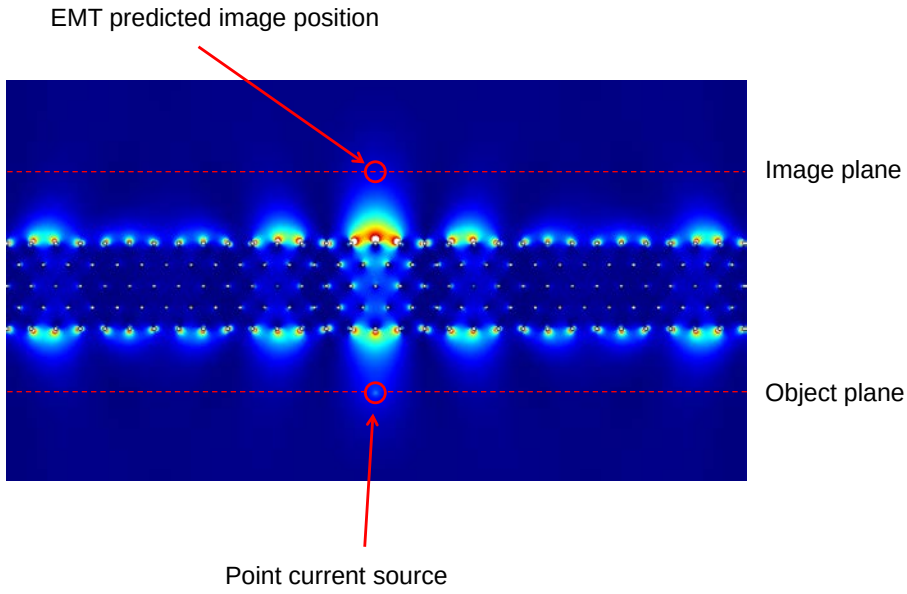


Fig. 4.6 (a) The electric field map ($|E|^2$) of full-wave simulations of imaging of a point current source by the 5-layer NIM lens, where the object and image planes are symmetrically placed at twice the lens thickness. The geometry is surrounded by absorbing perfectly matched layers (PMLs). Note that there is no apparent image of the point source at the opposite location in the image plane.

Figure 4.7(a) shows that EMT underestimates the width of the central peak, as well as the relative amplitude of the side lobes. In contrast, the agreement of the microscopic model prediction with full-wave simulations is significantly improved. For example, *T* from the microscopic model accurately predicts the profile of the central peak. Although

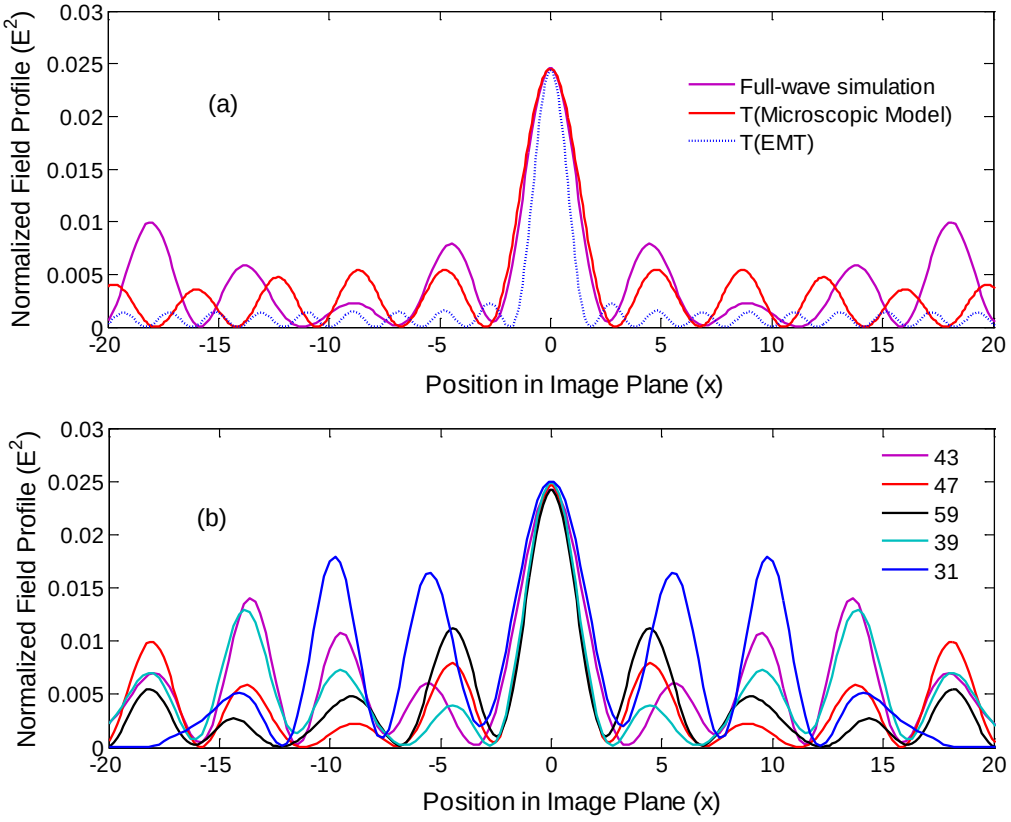


Fig. 4.7 (a) Normalized image profiles predicted by transmission calculated in both the microscopic and effective medium theory models, compared with the result from full-wave simulations. (b) Comparison of image profiles from full-wave simulations of lenses with different widths. The different profiles are marked by lens width in number of surface periods. The horizontal axis corresponds to the dimensionless *x*-position along the lens width.

the microscopic model provides improved agreement for the side lobes compared with EMT in terms of both amplitude and periodicity, the difference is non-negligible. This may be attributed to the finite width of the lens. We have performed further full-wave simulations of the image profile using structured NIM lenses of varying widths, with the results shown in Fig. 4.7(b). For different lens widths, the profile of the central peak is reproduced accurately, or with only slight broadening. However, the side lobes, especially their relative amplitudes, strongly depend on the lens width. This dependence may be due to the different stationary waves that these slabs support [114]. The narrowest lens (31 surface periods wide) corresponds to particularly intense side lobes close to the central one, which indicates the presence of strong edge effects.

## 4. 4 Implications on Perfect Lens and Modeling Metamaterials

The perfect lens was predicted based on EMT for the case of $\varepsilon=\mu=-1$. However, it was also recognized that such materials do not exist in nature and “no scheme can be of much interest if the means of realizing it are not available” [27]. To partly overcome this difficulty, a superlens using Ag [136, 137] with only negative $\varepsilon$ was devised in Ref. [27]. In the interpretation of subsequent NIM negative refraction experiments [38, 41, 42], assigning both negative $\varepsilon_{eff}$ and $\mu_{eff}$ to the composites through homogenization is intuitively appealing and generally accepted to have bridged this logical gap [43]. Therefore the "double negativity" interpretation of these experiments and the EMT in Ref. [27] together constitute the theoretical basis for constructing a perfect lens.

However, we showed in Sec. 2.4 that negative refraction observed from both periodic NIMs [38, 41, 42] and photonic crystals [44] can be given a unified, quantitative explanation based on a generalized phase matching condition, and the negative index, $n$, can be predicted from the complex Bloch band structure, without invoking either $\varepsilon_{eff}$ or $\mu_{eff}$ for the composite. Hence one can use either a microscopic theory or EMT to describe the same electromagnetic interaction between a point light source and a NIM slab. The question concerning perfect lensing is whether the transmission through the "double negative" composite as a function of $k_x$ behaves as predicted from EMT [27]. The microscopic approach shows that EMT significantly overestimates the range of $k_x$ that can be restored, hence limiting the achievable resolution. The deviation of EMT predicted transmission in terms of both amplitude and phase also leads to an underestimate of the image aberration due to the appearance of the intense side lobe diffraction. Therefore, based on the accurate microscopic model, it is unclear whether NIMs will lead to a superior optical imaging device.

The inadequacy of homogenization and EMT discussed here can be confusing, given the analogy between unit cells of metamaterial composites and molecules of conventional dielectrics in nature: $\varepsilon$ and $\mu$ for natural dielectrics are also an approximate result of homogenization, but their macroscopic Maxwell's Equations are considered exact. However, as was discussed in Sec. 1.1, these equations are only applicable in experiments that probe macroscopic electromagnetic fields. In other cases microscopic models such as X-ray diffraction theory are used. Moreover, $\varepsilon$ and $\mu$ for conventional dielectrics are sufficiently accurate for predicting *all* macroscopic experimental observations.

In contrast, experiments on metamaterials often focus on a single effect, where the boundaries between the above different length scales also tend to be more ambiguous. The failure of the EMT prediction of perfect lensing can be understood as the result of applying a macroscopic model to an intrinsically microscopic effect, since the involvement of all evanescent waves in $k$ space implies a lack of microscopic cutoff in real space.

## 4. 5 Summary

We have shown that microstructure leads to an overestimate of the range of evanescent waves within the first SBZ that can be recovered by an idealized $\varepsilon=\mu=-1$ model lossless metamaterial, when EMT is used to model a NIM slab. This is confirmed by observed broadening of the central peak in numerically simulated image profile of a point source. As such, perfect lensing [27] may not be experimentally possible using composite structures, even when the unit cell periodicity is significantly subwavelength.

# CHAPTER 5

## Conclusions and Future of Metamaterials

This chapter summarizes the approaches and results in this dissertation to answer the five questions in Sec. 1.7. We also reflect on homogenization and provide a view of our perspectives on the future of metamaterials research.

### 5. 1 Summary of Thesis

In Chapter 2, the design of a subwavelength near-infrared NIM using paired metallic strips is presented. A maximum unit cell size and a general relation between the bulk refractive index of an *arbitrary* NIM and its photonic band structure are derived in the zero-loss limit. The effective index is given by $n_{eff} = (k/k_0)\,\mathrm{sgn}(\partial\omega/\partial\,\mathrm{Re}(k))$. Based on discrete translational symmetry, we generalize Bloch's theorem to a phase matching condition with a complex transverse wavevector. Using the generalized phase matching condition, we provide a unified explanation of negative refraction observed in both lossless photonic crystals and lossy NIMs. The generality of this phase matching approach implies that it applies to wave phenomena other than electromagnetism, and the media on either side of the interface may be homogeneous or periodic. The analytical

results are then tested in a number of ways, including numerical simulations of NIM prisms, optical and microwave frequency NIM refraction experiments, as well as quantum mechanical and acoustics experiments in the literature.

In Chapter 3, the subwavelength near-infrared NIM introduced in Chapter 2 is fabricated using electron beam lithography. The NIM has a ratio of wavelength to periodicity of 7, the highest among known experimental optical NIMs. The NIM is then characterized by scanning electron and atomic force microscopies and optical transmission measurements. A negative phase advance through this NIM is observed through interferometry. All these measurements are consistent with a bulk negative index calculated from the photonic band structure of the NIM.

In Chapter 4, we design a model NIM based on localized Mie resonances in cylinders with a positive $\varepsilon$ and $\mu$. After homogenization, the composite is shown to be a material exhibiting $\varepsilon=\mu=-1$ in the effective medium theory (EMT). Transmission of plane waves through such a flat NIM lens is calculated using both EMT and a microscopic model that preserves the NIM's internal structure, and further used to predict the image profile of a point light source. By comparing both results with full-wave simulations, we find that EMT substantially overestimates the range of recoverable evanescent waves due to neglect of the microstructure. This implies that perfect lensing may not be experimentally attainable, even if the NIMs are significantly subwavelength.

## 5. 2 Reflections on Homogenization and Future of Metamaterials Research

In research on metamaterials, the model of effective medium has been successful in explaining many observations, and its predictions have been instrumental in

hypothesizing possible applications of composites. These predictions, however, often involve mathematical singularities, as well as $\varepsilon$ and $\mu$ that are extreme and uncommon [27, 35]. Nevertheless, considerable effort has been devoted to developing a unified homogenization theory to assign $\varepsilon_{eff}$ and $\mu_{eff}$ to an *arbitrary* composite, so that EMT predictions of the performance of a macroscopic device are generally effective. It is, therefore, often assumed that metamaterials with subwavelength unit cells can be homogenized and described by $\varepsilon_{eff}$ and $\mu_{eff}$.

Our work in Chapter 4 has shown that this assumption may not apply to metamaterials, and the use of EMT may lead to significant deviations from observation due to the neglect of microstructure, at least for some effects of particular interest. Indeed, we derived in Sec. 2.2 a maximum periodicity, below which a NIM behaves as a homogeneous medium in refraction experiments in the zero-loss limit. A NIM with a more relaxed periodicity may still have subwavelength unit cells, but it behaves as a grating with multiple diffraction orders in the far field. Such phenomena have been observed in experiments [61, 68]. Apparently, any homogenization theory applied to such NIMs leads to an inaccurate description in $\varepsilon_{eff}$ and $\mu_{eff}$.

A related, long-standing question on metamaterials that is of significant interest to experimentalists is how small a unit cell is small enough, which has led to varying speculations since as early as Lewin's homogenization work in 1947 [5, 59, 124, 128]. A more definitive version of this question is whether it is possible to derive a general maximum unit cell size for EMT to be effective for *every* effect on an arbitrary metamaterial. A homogenization theory applied with such a criterion may still be considered general. If such a size exists, experimentalists may therefore choose any unit

cells with the required $\varepsilon_{eff}$ and $\mu_{eff}$ below this maximum size for ease of implementation. This general maximum unit cell size, however, may not exist. We illustrate this point with the diagram in Fig. 5.1, where three circles correspond to the different sets of metamaterials for which the three types of experimental observations are possible: far-field scattering parameter measurements, negative refraction, and perfect lensing. Since far-field transmission and reflection can always be measured for any material, every composite is in the corresponding circle, which is also implied by its dashed boundary. For negative refraction, the maximum unit cell size in Sec. 2.2 sets a limit for zero-loss NIMs, hence the corresponding circle includes only some composites. Finally, our work in Chapter 4 and all experimental work so far indicate that it is still unknown whether any physical material is in the central circle and can be used to make a perfect lens. This diagram shows that different effects correspond to different critical length scales, even if these critical scales can be defined.

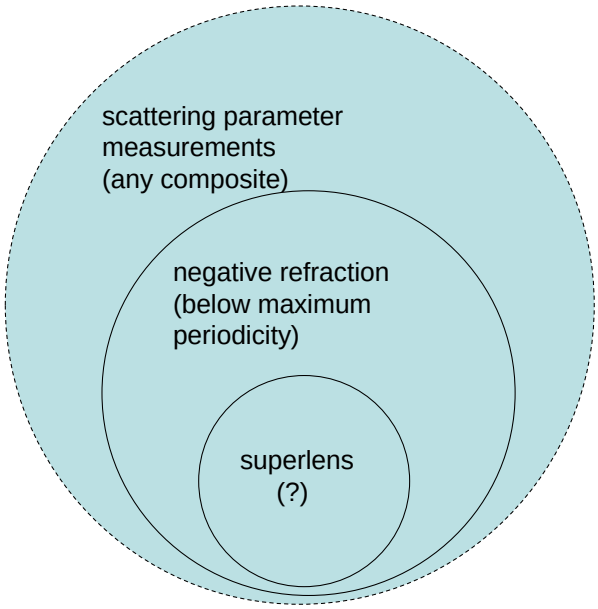


Fig. 5.1 Circles that correspond to maximum metamaterial unit cell sizes for different phenomena.

Therefore it is unlikely that there exists a universal homogenization theory, nor a general maximum unit cell size. Unlike macroscopic Maxwell's equations that can replace experiments to a great extent in antenna research, homogenization and EMT are not a substitute for experimental study of metamaterial composites. There does not seem to be a shortcut for solving this fundamental problem, which is dictated by the empirical nature of Maxwell's equations, as discussed in Sec. 1.1.

It is therefore important to ensure that the particular physical behavior of the metamaterial is consistent with predictions from EMT. Microscopic models, as an intermediate step between EMT and experimental implementations, may serve as a sanity check and answer practical questions such as whether reducing loss is sufficient for achieving a specific application. Although experimental study and microscopic modeling have not dominated the literature, they are expected to be the central theme of metametarials research in the ensuing years.

# Bibliography


1. G. Russakof, "A Derivation of Macroscopic Maxwell Equations," Am. J. Phys. **38**, 1188 (1970).

2. J. D. Jackson, *Classical Electrodynamics* (John Wiley & Sons, New York, 1998).

3. L. D. Landau, and E. M. Lifshitz, *Electrodynamics of Continuous Media* (Pergamon, Oxford, 1984).

4. R. Merlin, "Metamaterials and the Landau-Lifshitz permeability argument: Large permittivity begets high-frequency magnetism," Proc. Natl. Acad. Sci. U. S. A. **106**, 1693-1698 (2009).

5. G. M. Milton, *The Theory of Composites* (Cambridge University Press, Cambridge, 1995).

6. V. G. Veselago, "Electrodynamics of Substances with Simultaneously Negative Values of $\varepsilon$ and $\mu$ " Soviet Physics Uspekhi-Ussr **10**, 509 (1968).

7. V. G. Veselago, and E. E. Narimanov, "The left hand of brightness: past, present and future of negative index materials," Nat. Mater. **5**, 759-762 (2006).

8. H. Lamb, "On group-velocity," Proc. London Math. Soc. **1**, 473-479 (1904).

9. H. C. Pocklington, "Growth of a wave group when the group velocity is negative," Nature **71**, 607-608 (1905).

10. A. Schuster, *An Introduction to the Theory of Optics* (Edward Arnold, London, 1904).

11. L. I. Mandel'shtam, *Complete Collected Works* (Akad. Nauk SSSR, Moscow, 1947).

12. G. D. Malyuzhinets, "ZAMECHANIE PO POVODU PRINTSIPA IZLUCHENIYA," Zh. Tekh. Fiz. **21**, 940-942 (1951).

13. D. V. Sivukhin, "Electro-magnetic field energy in dispersing media " Opt. Spektrosk. **3**, 308-312 (1957).

14. V. E. Pafomov, "Transition radiation and Cerenkov radiation," Soviet Physics Jetp-Ussr **9**, 1321-1324 (1959).

15. J. B. Pendry, A. J. Holden, W. J. Stewart, and I. Youngs, "Extremely low frequency plasmons in metallic mesostructures," Phys. Rev. Lett. **76**, 4773-4776 (1996).

16. J. Brown, "Artificial dielectrics having refractive indices less than unity," Proceedings of the Institution of Electrical Engineers-London **100**, 51-62 (1953).

17. W. Rotman, "Plasma simulation by artificial dielectrics and parallel-plate media," IEEE Trans. Antennas Propag. **10**, 82-95 (1962).

18. S. A. Ramakrishna, "Physics of negative refractive index materials," Rep. Prog. Phys. **68**, 449-521 (2005).

19. D. F. Sievenpiper, M. E. Sickmiller, and E. Yablonovitch, "3D wire mesh photonic crystals," Phys. Rev. Lett. **76**, 2480-2483 (1996).

20. A. L. Pokrovsky, and A. L. Efros, "Electrodynamics of metallic photonic crystals and the problem of left-handed materials," Phys. Rev. Lett. **89**, 093901 (2002).

21. P. A. Belov, R. Marques, S. I. Maslovski, I. S. Nefedov, M. Silveirinha, C. R. Simovski, and S. A. Tretyakov, "Strong spatial dispersion in wire media in the very large wavelength limit," Phys. Rev. B **67**, 113103 (2003).

22. A. L. Pokrovsky, "Analytical and numerical studies of wire-mesh metallic photonic crystals," Phys. Rev. B **69**, 195108 (2004).

23. H. J. Schneider, and P. Dullenkopf, "Slotted tube resonator - new NMR probe head at high observing frequencies," Rev. Sci. Instrum. **48**, 68-73 (1977).

24. W. N. Hardy, and L. A. Whitehead, "Split-ring resonator for use in magnetic-resonance from 200-2000 mhz," Rev. Sci. Instrum. **52**, 213-216 (1981).

25. J. B. Pendry, A. J. Holden, D. J. Robbins, and W. J. Stewart, "Magnetism from conductors and enhanced nonlinear phenomena," IEEE Trans. Microw. Theory Tech. **47**, 2075-2084 (1999).

26. D. R. Smith, and J. B. Pendry, "Homogenization of metamaterials by field averaging (invited paper)," J. Opt. Soc. B **23**, 391-403 (2006).

27. J. B. Pendry, "Negative refraction makes a perfect lens," Phys. Rev. Lett. **85**, 3966-3969 (2000).

28. D. R. Smith, J. B. Pendry, and M. C. K. Wiltshire, "Metamaterials and negative refractive index," Science **305**, 788-792 (2004).

29. N. Engheta, and R. W. Ziolkowski, "A positive future for double-negative metamaterials," IEEE Trans. Microw. Theory Tech. **53**, 1535-1556 (2005).

30. C. M. Soukoulis, M. Kafesaki, and E. N. Economou, "Negative-index materials: New frontiers in optics," Advanced Materials **18**, 1941-1952 (2006).

31. V. M. Shalaev, "Optical negative-index metamaterials," Nature Photonics **1**, 41-48 (2007).

32. U. Leonhardt, and T. G. Philbin, "Transformation Optics and the Geometry of Light," in *Progress in Optics, Vol 53*(Elsevier Science Bv, Amsterdam, 2009), pp. 69-152.

33. H. Y. Chen, C. T. Chan, and P. Sheng, "Transformation optics and metamaterials," Nat. Mater. **9**, 387-396 (2010).

34. P. R. Berman, "Goos-Hanchen shift in negatively refractive media," Phys. Rev. E **66**, 067603 (2002).

35. J. B. Pendry, D. Schurig, and D. R. Smith, "Controlling electromagnetic fields," Science **312**, 1780-1782 (2006).

36. U. Leonhardt, "Optical conformal mapping," Science **312**, 1777-1780 (2006).

37. D. R. Smith, W. J. Padilla, D. C. Vier, S. C. Nemat-Nasser, and S. Schultz, "Composite medium with simultaneously negative permeability and permittivity," Phys. Rev. Lett. **84**, 4184-4187 (2000).

38. R. A. Shelby, D. R. Smith, and S. Schultz, "Experimental verification of a negative index of refraction," Science **292**, 77-79 (2001).

39. N. Garcia, and M. Nieto-Vesperinas, "Is there an experimental verification of a negative index of refraction yet?," Opt. Lett. **27**, 885-887 (2002).

40. P. M. Valanju, R. M. Walser, and A. P. Valanju, "Wave refraction in negative-index media: Always positive and very inhomogeneous," Phys. Rev. Lett. **88**, 187401 (2002).

41. C. G. Parazzoli, R. B. Greegor, K. Li, B. E. C. Koltenbah, and M. Tanielian, "Experimental verification and simulation of negative index of refraction using Snell's law," Phys. Rev. Lett. **90**, 107401 (2003).

42. R. B. Greegor, C. G. Parazzoli, K. Li, B. E. C. Koltenbah, and M. Tanielian, "Experimental determination and numerical simulation of the properties of negative index of refraction materials," Opt. Express **11**, 688-695 (2003).

43. J. Pendry, "Optics: Positively negative," Nature **423**, 22-23 (2003).

44. M. Notomi, "Theory of light propagation in strongly modulated photonic crystals: Refraction like behavior in the vicinity of the photonic band gap," Phys. Rev. B **62**, 10696-10705 (2000).

45. S. Zhang, W. J. Fan, N. C. Panoiu, K. J. Malloy, R. M. Osgood, and S. R. J. Brueck, "Experimental demonstration of near-infrared negative-index metamaterials," Phys. Rev. Lett. **95**, 137404 (2005).

46. V. M. Shalaev, W. S. Cai, U. K. Chettiar, H. K. Yuan, A. K. Sarychev, V. P. Drachev, and A. V. Kildishev, "Negative index of refraction in optical metamaterials," Opt. Lett. **30**, 3356 (2005).

47. D. Schurig, J. J. Mock, B. J. Justice, S. A. Cummer, J. B. Pendry, A. F. Starr, and D. R. Smith, "Metamaterial electromagnetic cloak at microwave frequencies," Science **314**, 977-980 (2006).

48. X. H. Zhang, M. Davanço, Y. Urzhumov, G. Shvets, and S. R. Forrest, "From Scattering Parameters to Snell's Law: A Subwavelength Near-Infrared Negative-Index Metamaterial," Phys. Rev. Lett. **101**, 267401 (2008).

49. X. H. Zhang, and S. R. Forrest, "Generalized phase matching condition for lossy periodic photonic structures," Opt. Express **18**, 1151-1158 (2010).

50. M. Davanço, X. H. Zhang, S. R. Forrest, Y. Urzhumov, and G. Shvets, "Nanofabrication and Characterization of Subwavelength Metamaterials for Negative-index Propagation at Near-infrared Wavelengths," Lasers and Electro-Optics Society, 2007. LEOS 2007. The 20th Annual Meeting of the IEEE, 325-326 (2007).

51. X. H. Zhang, M. Davanço, Y. Urzhumov, G. Shvets, and S. R. Forrest, " A Subwavelength Near-Infrared Negative-Index Material," Appl. Phys. Lett. **94**, 131107 (2009).

52. X. H. Zhang, M. Davanço, K. Maller, T. W. Jarvis, C. H. Wu, C. Fietz, D. Korobkin, X. Q. Li, G. Shvets, and S. R. Forrest, "Interferometric characterization of a sub-wavelength near-infrared negative index metamaterial," Opt. Express **18**, 17788-17795 (2010).

53. X. H. Zhang, and S. R. Forrest, "Theory of the perfect lens," submitted.

54. D. R. Smith, S. Schultz, P. Markos, and C. M. Soukoulis, "Determination of effective permittivity and permeability of metamaterials from reflection and transmission coefficients," Phys. Rev. B **65**, 195104 (2002).

55. T. Koschny, P. Markos, D. R. Smith, and C. M. Soukoulis, "Resonant and antiresonant frequency dependence of the effective parameters of metamaterials," Phys. Rev. E **68**, 065602 (2003).

56. C. M. Soukoulis, J. F. Zhou, T. Koschny, M. Kafesaki, and E. N. Economou, "The science of negative index materials," J. Phys.-Condes. Matter **20**, 304217 (2008).

57. G. Dolling, M. Wegener, and S. Linden, "Realization of a three-functional-layer negative-index photonic metamaterial," Opt. Lett. **32**, 551-553 (2007).

58. C. Rockstuhl, T. Paul, F. Lederer, T. Pertsch, T. Zentgraf, T. P. Meyrath, and H. Giessen, "Transition from thin-film to bulk properties of metamaterials," Phys. Rev. B **77**, 035126 (2008).

59. T. Koschny, P. Markos, E. N. Economou, D. R. Smith, D. C. Vier, and C. M. Soukoulis, "Impact of inherent periodic structure on effective medium description of left-handed and related metamaterials," Phys. Rev. B **71**, 245105 (2005).

60. H. J. Lezec, J. A. Dionne, and H. A. Atwater, "Negative refraction at visible frequencies," Science **316**, 430-432 (2007).

61. A. A. Houck, J. B. Brock, and I. L. Chuang, "Experimental observations of a left-handed material that obeys Snell's law," Phys. Rev. Lett. **90**, 137401 (2003).

62. J. Yao, Z. W. Liu, Y. M. Liu, Y. Wang, C. Sun, G. Bartal, A. M. Stacy, and X. Zhang, "Optical negative refraction in bulk metamaterials of nanowires," Science **321**, 930-930 (2008).

63. V. Lomakin, Y. Fainman, Y. Urzhumov, and G. Shvets, "Doubly negative metamaterials in the near infrared and visible regimes based on thin film nanocomposites," Opt. Express **14**, 11164-11177 (2006).

64. E. D. Palik, *Handbook of optical constants of solids* (Academic Press, Orlando, 1985).

65. M. Davanço, Y. Urzhumov, and G. Shvets, "The Complex Bloch Bands of a 2D Plasmonic Crystal Displaying Isotropic Negative Refraction," Opt. Express **15**, 9681-9691 (2007).

66. D. Seetharamdoo, R. Sauleau, K. Mahdjoubi, and A. C. Tarot, "Effective parameters of resonant negative refractive index metamaterials: Interpretation and validity," J. Appl. Phys. **98**, 063505 (2005).

67. P. Yeh, "Electromagnetic Propagation in Birefringent Layered Media," Journal of the Optical Society of America **69**, 742-756 (1979).

68. D. R. Smith, P. M. Rye, J. J. Mock, D. C. Vier, and A. F. Starr, "Enhanced diffraction from a grating on the surface of a negative-index metamaterial," Phys. Rev. Lett. **93**, 137405 (2004).

69. D. R. Smith, D. C. Vier, T. Koschny, and C. M. Soukoulis, "Electromagnetic parameter retrieval from inhomogeneous metamaterials," Phys. Rev. E **71**, 036617 (2005).

70. J. Valentine, S. Zhang, Z. T., E. Ulin-Avila, G. D.A., G. Bartal, and X. Zhang, "Three-dimensional optical metamaterial with a negative refractive index," Nature **455**, 376 (2008).

71. A. Mary, R. S.G., G.-V. F.J., and M.-M. L, "Theory of Negative-Refractive-Index Response of Double-Fishnet Structures," Phys. Rev. Lett. **101**, 103902 (2008).

72. J. D. Joannopoulos, R. D. Meade, and J. N. Winn, *Photonic Crystals: Molding the Flow of Light* (Princeton University Press, Princeton and Oxford, 2008).

73. A. Damascelli, Z. Hussain, and Z. X. Shen, "Angle-resolved photoemission studies of the cuprate superconductors," Rev. Mod. Phys. **75**, 473-541 (2003).

74. C. Luo, S. G. Johnson, J. D. Joannopoulos, and J. B. Pendry, "All-angle negative refraction without negative effective index," Phys. Rev. B **65**, 201104 (2002).

75. J. B. Pendry, "Photonic Band Structures," J. Mod. Opt. **41**, 209-229 (1994).

76. D. de Ceglia, M. A. Vincenti, M. G. Cappeddu, M. Centini, N. Akozbek, A. D'Orazio, J. W. Haus, M. J. Bloemer, and M. Scalora, "Tailoring metallodielectric structures for superresolution and superguiding applications in the visible and near-ir ranges," Phys. Rev. A **77**, 033848 (2008).

77. C. Rockstuhl, C. Menzel, T. Paul, T. Pertsch, and F. Lederer, "Light propagation in a fishnet metamaterial," Phys. Rev. B **78**, 155102 (2008).

78. R. A. Shelby, D. R. Smith, S. C. Nemat-Nasser, and S. Schultz, "Microwave transmission through a two-dimensional, isotropic, left-handed metamaterial," Appl. Phys. Lett. **78**, 489-491 (2001).

79. K. Sakoda, *Optical Properties of Photonic Crystals* (Springer, Berlin, 2001).

80. N. W. Ashcroft, and N. D. Mermin, *Solid State Physics* (Holt, Rinehart and Winston, New York, 1976).

81. P. C. Clemmow, *The Plane Wave Spectrum Representation of Electromagnetic Fields* (Pergamon Press, Oxford and New York, 1966).

82. N. F. Declercq, J. Degrieck, and O. Leroy, "The Laplace transform to describe bounded inhomogeneous waves," J. Acoust. Soc. Am. **116**, 51-60 (2004).

83. W. Huang, R. Briers, S. I. Rokhlin, and O. Leroy, "Experimental-Study of Inhomogeneous Wave Reflection from a Solid-Air Periodically Rough Boundary Using Leaky Rayleigh-Waves," J. Acoust. Soc. Am. **96**, 363-369 (1994).

84. R. Briers, O. Leroy, O. Poncelet, and M. Deschamps, "Experimental verification of the calculated diffraction field generated by inhomogeneous waves obliquely incident on a periodically rough liquid-solid boundary," J. Acoust. Soc. Am. **106**, 682-687 (1999).

85. N. F. Declercq, R. Briers, J. Degrieck, and O. Leroy, "The history and properties of ultrasonic inhomogeneous waves," IEEE Trans. Ultrason., Ferroelectr., Freq. Control **52**, 776-791 (2005).

86. R. B. Greegor, C. G. Parazzoli, K. Li, and M. H. Tanielian, "Origin of dissipative losses in negative index of refraction materials," Appl. Phys. Lett. **82**, 2356-2358 (2003).

87. K. Li, S. J. McLean, R. B. Greegor, C. G. Parazzoli, and M. H. Tanielian, "Free-space focused-beam characterization of left-handed materials," Appl. Phys. Lett. **82**, 2535-2537 (2003).

88. M. Notomi, "Manipulating light with strongly modulated photonic crystals," Rep. Prog. Phys. **73**, 096501 (2010).

89. S. Foteinopoulou, and C. M. Soukoulis, "Negative refraction and left-handed behavior in two-dimensional photonic crystals," Phys. Rev. B **67**, 235107 (2003).

90. I. Tsukerman, "Negative refraction and the minimum lattice cell size," J. Opt. Soc. B **25**, 927-936 (2008).

91. N. Liu, H. C. Guo, L. W. Fu, S. Kaiser, H. Schweizer, and H. Giessen, "Three-dimensional photonic metamaterials at optical frequencies," Nat. Mater. **7**, 31-37 (2008).

92. Y. A. Urzhumov, and G. Shvets, "Optical magnetism and negative refraction in plasmonic metamaterials," Solid State Commun. **146**, 208-220 (2008).

93. B. Kante, J. M. Lourtioz, and A. de Lustrac, "Infrared metafilms on a dielectric substrate," Phys. Rev. B **80**, 205120 (2009).

94. G. Dolling, C. Enkrich, M. Wegener, C. M. Soukoulis, and S. Linden, "Simultaneous negative phase and group velocity of light in a metamaterial," Science **312**, 892-894 (2006).

95. G. D'Aguanno, M. Centini, M. Scalora, C. Sibilia, M. J. Bloemer, C. M. Bowden, J. W. Haus, and M. Bertolotti, "Group velocity, energy velocity, and superluminal propagation in finite photonic band-gap structures," Phys. Rev. E **63**, 036610 (2001).

96. V. P. Drachev, W. Cai, U. Chettiar, H. K. Yuan, A. K. Sarychev, A. V. Kildishev, G. Klimeck, and V. M. Shalaev, "Experimental verification of an optical negative-index material," Laser Physics Letters **3**, 49-55 (2006).

97. Z. F. Li, K. Aydin, and E. Ozbay, "Determination of the effective constitutive parameters of bianisotropic metamaterials from reflection and transmission coefficients," Phys. Rev. E **79**, 026610 (2009).

98. J. F. Zhou, T. Koschny, L. Zhang, G. Tuttle, and C. M. Soukoulis, "Experimental demonstration of negative index of refraction," Appl. Phys. Lett. **88**, 221103 (2006).

99. J. A. Kong, *Electromagnetic Wave Theory* (EMW, Cambridge, MA, 2008).

100. A. Grbic, and G. V. Eleftheriades, "Overcoming the diffraction limit with a planar left-handed transmission-line lens," Phys. Rev. Lett. **92**, 117403 (2004).

101. J. Zhu, and G. V. Eleftheriades, "Experimental verification of overcoming the diffraction limit with a volumetric Veselago-Pendry transmission-line lens," Phys. Rev. Lett. **101**, 013902 (2008).

102. K. Aydin, I. Bulu, and E. Ozbay, "Subwavelength resolution with a negative-index metamaterial superlens," Appl. Phys. Lett. **90**, 254102 (2007).

103. R. Chatterjee, N. C. Panoiu, K. Liu, Z. Dios, M. B. Yu, M. T. Doan, L. J. Kaufman, R. M. Osgood, and C. W. Wong, "Achieving subdiffraction imaging through bound surface states in negative refraction photonic crystals in the near-infrared range," Phys. Rev. Lett. **100**, 187401 (2008).

104. A. K. Iyer, and G. V. Eleftheriades, "Free-Space Imaging Beyond the Diffraction Limit Using a Veselago-Pendry Transmission-Line Metamaterial Superlens," IEEE Trans. Antennas Propag. **57**, 1720-1727 (2009).

105. F. Keilmann, and R. Hillenbrand, "Near-field microscopy by elastic light scattering from a tip," Philos. Trans. R. Soc. Lond. Ser. A-Math. Phys. Eng. Sci. **362**, 787-805 (2004).

106. R. W. Ziolkowski, and E. Heyman, "Wave propagation in media having negative permittivity and permeability," Phys. Rev. E **64**, 056625 (2001).

107. N. Garcia, and M. Nieto-Vesperinas, "Left-handed materials do not make a perfect lens," Phys. Rev. Lett. **88**, 207403 (2002).

108. D. R. Smith, D. Schurig, M. Rosenbluth, S. Schultz, S. A. Ramakrishna, and J. B. Pendry, "Limitations on subdiffraction imaging with a negative refractive index slab," Appl. Phys. Lett. **82**, 1506-1508 (2003).

109. S. A. Cummer, "Simulated causal subwavelength focusing by a negative refractive index slab," Appl. Phys. Lett. **82**, 1503-1505 (2003).

110. V. A. Podolskiy, and E. E. Narimanov, "Near-sighted superlens," Opt. Lett. **30**, 75-77 (2005).

111. L. Peng, L. X. Ran, H. S. Chen, H. F. Zhang, J. A. Kong, and T. M. Grzegorczyk, "Experimental observation of left-handed behavior in an array of standard dielectric resonators," Phys. Rev. Lett. **98**, 157403 (2007).

112. S. M. Xiao, V. P. Drachev, A. V. Kildishev, X. J. Ni, U. K. Chettiar, H. K. Yuan, and V. M. Shalaev, "Loss-free and active optical negative-index metamaterials," Nature **466**, 735-U736 (2010).

113. F. D. M. Haldane, cond-mat/0206420 (unpublished).

114. A. Grbic, and G. V. Eleftheriades, "Practical limitations of subwavelength resolution using negative-refractive-index transmission-line lenses," IEEE Trans. Antennas Propag. **53**, 3201-3209 (2005).

115. C. Menzel, T. Paul, C. Rockstuhl, T. Pertsch, S. Tretyakov, and F. Lederer, "Validity of effective material parameters for optical fishnet metamaterials," Phys. Rev. B **81**, 035320 (2010).

116. S. B. Raghunathan, and N. V. Budko, "Effective permittivity of finite inhomogeneous objects," Phys. Rev. B **81**, 054206 (2010).

117. A. P. McCauley, R. K. Zhao, M. T. H. Reid, A. W. Rodriguez, J. F. Zhou, F. S. S. Rosa, J. D. Joannopoulos, D. A. R. Dalvit, C. M. Soukoulis, and S. G. Johnson, "Microstructure effects for Casimir forces in chiral metamaterials," Phys. Rev. B **82**, 165108 (2010).

118. R. Zhao, J. Zhou, T. Koschny, E. N. Economou, and C. M. Soukoulis, "Repulsive Casimir Force in Chiral Metamaterials," Phys. Rev. Lett. **103**, 103602 (2009).

119. K. Vynck, D. Felbacq, E. Centeno, A. I. Cabuz, D. Cassagne, and B. Guizal, "All-Dielectric Rod-Type Metamaterials at Optical Frequencies," Phys. Rev. Lett. **102**, 133901 (2009).

120. R. L. Chern, and Y. T. Chen, "Effective parameters for photonic crystals with large dielectric contrast," Phys. Rev. B **80**, 075118 (2009).

121. S. Y. Liu, W. K. Chen, J. J. Du, Z. F. Lin, S. T. Chui, and C. T. Chan, "Manipulating Negative-Refractive Behavior with a Magnetic Field," Phys. Rev. Lett. **101**, 157407 (2008).

122. C. Fietz, and G. Shvets, "Current-driven metamaterial homogenization," Physica B **405**, 2930-2934 (2010).

123. P. Sheng, *Introduction to Wave Scattering, Localization, and Mesoscopic Phenomena* (AcademicPress, San Diego, 1995).

124. L. Lewin, "The electrical constants of a material loaded with spherical particles," Proc. Inst. Electr. Eng. **94**, 65 (1947).

125. N. A. Khizhnyak, "Artificial anisotropic dielectrics formed from two-dimensional lattices of infinite bars and rods," Sov. Phys. Tech. Phys. **29**, 604-614 (1959).

126. D. Stroud, and F. P. Pan, "Self-consistent approach to electromagnetic-wave propagation in composite media - application to model granular metals," Phys. Rev. B **17**, 1602-1610 (1978).

127. P. C. Waterman, and N. E. Pedersen, "Electromagnetic scattering by periodic arrays of particles," J. Appl. Phys. **59**, 2609-2618 (1986).

128. C. L. Holloway, E. F. Kuester, J. Baker-Jarvis, and P. Kabos, "A double negative (DNG) composite medium composed of magnetodielectric spherical particles embedded in a matrix," IEEE Trans. Antennas Propag. **51**, 2596-2603 (2003).

129. Y. Q. Ding, Z. Y. Liu, C. Y. Qiu, and J. Shi, "Metamaterial with simultaneously negative bulk modulus and mass density," Phys. Rev. Lett. **99**, 093904 (2007).

130. Y. Wu, J. Li, Z. Q. Zhang, and C. T. Chan, "Effective medium theory for magnetodielectric composites: Beyond the long-wavelength limit," Phys. Rev. B **74**, 085111 (2006).

131. C. Y. Luo, S. G. Johnson, J. D. Joannopoulos, and J. B. Pendry, "Subwavelength imaging in photonic crystals," Phys. Rev. B **68**, 045115 (2003).

132. R. Ruppin, "Surface polaritons of a left-handed material slab," J. Phys.-Condes. Matter **13**, 1811-1818 (2001).

133. B. J. Soller, H. R. Stuart, and D. G. Hall, "Energy transfer at optical frequencies to silicon-on-insulator structures," Opt. Lett. **26**, 1421-1423 (2001).

134. S. L. He, Z. C. Ruan, L. Chen, and J. Q. Shen, "Focusing properties of a photonic crystal slab with negative refraction," Phys. Rev. B **70**, 115113 (2004).

135. M. Inoue, K. Ohtaka, and S. Yanagawa, "Light-scattering from macroscopic spherical bodies .2. reflectivity of light and electromagnetic localized state in a periodic monolayer of dielectric spheres," Phys. Rev. B **25**, 689-699 (1982).

136. N. Fang, H. Lee, C. Sun, and X. Zhang, "Sub-diffraction-limited optical imaging with a silver superlens," Science **308**, 534-537 (2005).

137. P. Chaturvedi, W. Wu, V. J. Logeeswaran, Z. N. Yu, M. S. Islam, S. Y. Wang, R. S. Williams, and N. X. Fang, "A smooth optical superlens," Appl. Phys. Lett. **96**, 043102 (2010).